

GROWTH, CHARACTERIZATION AND FABRICATION OF ALGAN/GAN
HIGH ELECTRON MOBILITY TRANSISTORS ON SILICON CARBIDE
SUBSTRATES

A THESIS SUBMITTED TO
THE GRADUATE SCHOOL OF NATURAL AND APPLIED SCIENCES
OF
MIDDLE EAST TECHNICAL UNIVERSITY

BY

AYÇA EMEN

IN PARTIAL FULFILLMENT OF THE REQUIREMENTS
FOR
THE DEGREE OF MASTER OF SCIENCE
IN
MICRO AND NANOTECHNOLOGY

JANUARY 2014

Approval of the thesis:

**GROWTH, CHARACTERIZATION AND FABRICATION OF
ALGAN/GAN HIGH ELECTRON MOBILITY TRANSISTORS ON
SILICON CARBIDE SUBSTRATES**

submitted by **AYÇA EMEN** in partial fulfillment of the requirements for the degree of **Master of Science in Micro and Nanotechnology Department, Middle East Technical University** by,

Prof. Dr. Canan Özgen _____
Dean, Graduate School of **Natural and Applied Sciences**

Prof. Dr. Tayfun Akın _____
Head of Department, **Micro and Nanotechnology**

Assoc. Prof. Dr. Hüsnü Emrah Ünalın _____
Supervisor, **Metallurgical and Materials Eng., METU**

Prof. Dr. Raşit Turan _____
Co-supervisor, **Physics Dept., METU**

Examining Committee Members:

Prof. Dr. Raşit Turan _____
Physics Dept., METU

Assoc. Prof. Dr. Hüsnü Emrah Ünalın _____
Metallurgical and Materials Eng. Dept., METU

Prof. Dr. Ekmel Özbay _____
Physics Dept., BILKENT UNIVERSITY

Assist. Prof. Dr. Alpan Bek _____
Physics Dept., METU

Assist. Prof. Dr. Yunus Eren Kalay _____
Metallurgical and Materials Eng. Dept., METU

Date: _____

I hereby declare that all information in this document has been obtained and presented in accordance with academic rules and ethical conduct. I also declare that, as required by these rules and conduct, I have fully cited and referenced all material and results that are not original to this work.

Name, Last Name: AYÇA EMEN

Signature :

ABSTRACT

GROWTH, CHARACTERIZATION AND FABRICATION OF ALGAN/GAN HIGH ELECTRON MOBILITY TRANSISTORS ON SILICON CARBIDE SUBSTRATES

Emen, Ayça

M.S., Department of Micro and Nanotechnology

Supervisor : Assoc. Prof. Dr. Hüsnü Emrah Ünalan

Co-Supervisor : Prof. Dr. Raşit Turan

January 2014, 78 pages

Wide bandgap semiconductor technology for electronics have received great attention over the last several years. Heterostructures composed of aluminium gallium nitride (AlGaN) and gallium nitride (GaN) are promising candidates for the fabrication of high power and high frequency devices due to their superior material properties. Silicon carbide (SiC) is the most suitable substrate for GaN growth because of its high thermal conductivity and lower lattice mismatch with GaN compared to silicon and sapphire. This thesis investigates the epitaxial growth of AlGaN/GaN heterostructures using metal organic chemical vapor deposition (MOCVD) on 6H-SiC substrates and further application of these heterostructures as high electron mobility transistor (HEMT) devices. In the first part of the thesis, the growth of highly resistive GaN on SiC was optimized. Resistivity values as high as $10^{11} \Omega/\square$ was obtained from electrical measurements. Secondly, on the optimized GaN buffer, AlGaN/GaN heterostructures with different aluminium contents from 17 to 31% were grown. Structural

and electrical characterizations have been done. Heterostructures revealed full width half maximum (FWHM) values of ~ 300 and ~ 350 arcsec for GaN and AlGaN, respectively, indicating a good crystal quality. Furthermore, the two dimensional electron gas (2DEG) mobilities between 1150-1643 $\text{cm}^2/\text{V.s}$, sheet carrier concentrations on the order of 10^{13} cm^{-2} and sheet resistance values between 273 and 464 Ω/\square were obtained. Finally, HEMT devices were fabricated from AlGaN/GaN heterostructures and DC output and transfer characteristics were measured. The AlGaN/GaN HEMT device with an aluminium content of 31% exhibited maximum drain current density of 1210 mA/mm, while a peak transconductance of 288 mS/mm and breakdown voltage of 14 V was achieved.

Keywords: Epitaxial growth, microfabrication, MOCVD, HEMT, AlGaN/GaN HEMT

ÖZ

ALGAN/GAN YÜKSEK ELEKTRON MOBİLİTELİ TRANSİSTÖRLERİN SİLİSYUM KARBÜR ALTTAŞLAR ÜZERİNE BÜYÜTÜLMESİ, KARAKTERİZASYONU VE FABRİKASYONU

Emen, Ayça

Yüksek Lisans, Mikro ve Nanoteknoloji Bölümü

Tez Yöneticisi : Doç. Dr. Hüsnü Emrah Ünalan

Ortak Tez Yöneticisi : Prof. Dr. Raşit Turan

Ocak 2014 , 78 sayfa

Geniş bant aralığına sahip yarı iletken teknolojisi geçtiğimiz yıllarda mikroeletirik uygulamalar için oldukça ilgi çekmiştir. Üstün materyal özellikleri sayesinde alüminyum galyum nitrid (AlGaN) ve galyum nitrid (GaN) heteroeklemler yüksek güç ve yüksek frekans aygıt üretimi için en çok umut vaat eden adaylardır. Silikon karbür (SiC) , silikon ve safire kıyasla yüksek ısı iletkenliğine ve GaN ile düşük örgü uyumsuzluğuna sahip olması nedeni ile GaN büyütmeleri için en uygun alttaştır. Bu tezde AlGaN/GaN heteroeklem yapılarının metal organik buhar fazı epitaksi yöntemi ile büyütülmesi ve yüksek elektron mobiliteli tansistör aygıtları olarak fabrikasyonu üzerine çalışılmıştır. Tezin ilk bölümünde SiC alttaş üzerine yüksek dirençli GaN büyütmesi optimize edilmiştir. Elektriksel ölçümler sonucunda $10^{11} \Omega/\square$ kadar yüksek GaN tabaka direnci elde edilmiştir. İkinci olarak, optimize edilen GaN tampon tabakası üzerine, alüminyum oranı %17 den 31'e değişen AlGaN/GaN heteroeklem yapıları büyütülmüştür. Yapı-

sal ve elektriksel karakterizasyonlar gerçekleştirilmiştir. X-ışını difraktometresi taramaları; heteroeklemlerin GaN ve AlGaN için sırasıyla ~ 300 ve ~ 350 ark saniye yarı maksimumdaki tam genişlik değerleri ile iyi bir kristal kalitesine sahip olduğunu doğrulamıştır. Ek olarak, 2 boyutlu elektron gazı (2BEG) mobilite değerleri $1150-1643 \text{ cm}^2/\text{V.s}$ arasında, tabaka taşıyıcı konsantrasyon değerleri 10^{13} cm^{-2} mertebesinde ve tabaka direnç değerleri $273-464 \Omega/\square$ arasında elde edilmiştir. Son olarak, AlGaN /GaN yapıları HEMT aygıtlar olarak fabrike edilmiş ve doğru akım çıkış ve transfer karakteristikleri incelenmiştir. %31 alüminyum oranına sahip AlGaN /GaN aygıtından 1210 mA/mm maksimum akaç akım yoğunluğu, 288 mS/mm geçiş iletkenliği ve 14 V kırılma voltajı elde edilmiştir.

Anahtar Kelimeler: Epitaksiyel büyütme, mikrofabrikasyon, MOCVD, HEMT, AlGaN/GaN HEMT

To my mom...

ACKNOWLEDGMENTS

There are so many people give me strength during the journey of my thesis work. First of all, I would like to express my great gratitude to my supervisor Assoc. Professor Emrah Ünalın for his support, advices and valuable guidance throughout this study.

I also would like to thank my co-advisor Prof. Dr. Raşit Turan for his heartily support.

I am also thankful to Prof. Dr. Ekmel Özbay for his encouragement and support. It is a great pleasure to work with him. I also express my deepest gratitude for Dr. Özlem Şen, for her patience, valuable comments and guidance.

I would like to forward my appreciation to my former employer Mutlu Bayar for his support during the early stages of my thesis study.

I would like to thank my colleagues: Hüseyin Çakmak, Ömer Cengiz, Orkun Arıcan and Yıldırım Durmuş for their helps. I would like to give very special thanks to my valuable friends: Pakize Demirel, Doğan Yılmaz, Burak Turhan, Züleyha Artuç, Şeyda Şahiner and Ezgi Çalışkan for their endless motivation. My most willingly thanks are to my office mate Semih Çakmakyapan for his patience and invaluable help.

I am deeply indepted to my very important and valuable supporters, my family, Ayşe Teber, Aysun Emen and Çağrı Emen for always being with my side and support me during my life.

Finally, the presence of Alper Karadağ makes everything less burdensome, more amusing and bearable, without his support and love, it would have not been possible for me to finish this study.

TABLE OF CONTENTS

ABSTRACT	v
ÖZ	vii
ACKNOWLEDGMENTS	x
TABLE OF CONTENTS	xi
LIST OF TABLES	xii
LIST OF FIGURES	xiii
LIST OF ABBREVIATIONS	xiv
CHAPTERS	
1 INTRODUCTION	1
1.1 Basic Properties of III-Nitride Materials	3
1.2 AlGa _N /Ga _N heterostructures	5
1.2.1 High Electron Mobility Transistor (HEMT)	7
2 MOCVD GROWTH AND FABRICATION OF HEMT DEVICES	13
2.1 Metalorganic Chemical Vapor Deposition (MOCVD)	13
2.1.1 Setup of MOCVD System	16
2.1.2 Choice of Substrate	18
2.2 Material Characterization	19

2.2.1	In-situ characterization	19
2.2.2	Ex-situ layer characterization	21
2.2.2.1	High Resolution X-Ray Diffraction (HRXRD)	21
2.2.2.2	Hall Effect Measurements	23
2.2.2.3	Scanning Electron Microscopy (SEM)	25
2.2.2.4	Atomic Force Microscopy (AFM) .	26
2.3	Device Processing	27
2.3.1	Wafer preparation	27
2.3.2	Lithography	27
2.3.2.1	Optical Lithography	27
2.3.2.2	Electron Beam Lithography (EBL)	29
2.3.3	Etching	30
2.3.4	Metallization	30
2.3.5	Passivation	33
2.4	Device Characterization	34
2.4.1	Transmission Line Model	34
2.4.2	Ellipsometry	35
2.4.3	Direct Current Measurement	35
3	EXPERIMENTAL DETAILS	37
3.1	Epitaxial Growth of AlGaN/GaN HEMT Structures on SiC Substrates	37
3.1.1	Growth of Highly Resistive GaN Layer	37
3.1.2	Growth of Full HEMT Structure	40

3.2	Fabrication of HEMT devices	42
3.2.1	Sample Preparation	42
3.2.2	Mesa Isolation	43
3.2.3	Ohmic Contact Formation	43
3.2.4	Schottky Contact Formation	44
3.2.5	1st Level Metallization	45
3.2.6	Passivation	45
3.2.7	Contact Pad Opening	46
3.2.8	Air-Bridge Formation	47
3.2.9	Interconnect Metallization	48
4	RESULTS AND DISCUSSION	51
4.1	Characterization of Highly Resistive GaN structures on SiC	51
4.2	Characterization of AlGaN/GaN HEMT structures on GaN buffer	57
4.3	Characterizations of HEMT devices	63
4.4	DC Characterization of fabricated HEMT devices	65
5	CONCLUSIONS AND FUTURE WORK	69
	REFERENCES	71

LIST OF TABLES

TABLES

Table 1.1	Electrical Properties of Semiconductors [2].	2
Table 1.2	Lattice constants of group III-nitrides.	3
Table 2.1	Precursors for MOCVD [36].	15
Table 2.2	Properties of substrates that are available for III nitride epitaxy [39].	18
Table 3.1	The growth parameters of GaN on AlN layers.	40
Table 3.2	The growth parameters of the layers deposited onto highly resistive GaN buffer	41
Table 4.1	The AFM and HRXRD characterization results of highly resistive samples.	57
Table 4.2	The HRXRD ω scans of HEMT structures.	58
Table 4.3	The Hall Effect results of HEMT samples.	61
Table 4.4	Literature review of AlGaIn/GaN HEMT device performances.	68

LIST OF FIGURES

FIGURES

Figure 1.1	Bandgap energy vs lattice constant of III-V semiconductors at 300K [1].	1
Figure 1.2	Application areas of GaN transistors [3].	2
Figure 1.3	Hexagonal structure of wurtzite crystal.	4
Figure 1.4	Stick and ball stacking model of wurtzite and zincblende crystals [7].	4
Figure 1.5	Different polarities of wurtzite GaN.	5
Figure 1.6	Band diagram of the heterostructure formed by wide (I) and narrow (II) bandgap semiconductors at thermodynamic equilibrium [10].	6
Figure 1.7	Polarization induced sheet charge density in AlGaN/GaN heterostructure with N-face and Ga-face polarity.	7
Figure 1.8	Schematic HEMT structure.	9
Figure 2.1	The principle of MOCVD process [7].	16
Figure 2.2	Schematic of the reactor [37].	17
Figure 2.3	The configuration of in-situ characterization system [40].	19
Figure 2.4	Reflection of light from a substrate-layer system [41].	20
Figure 2.5	A typical reflectance transient [37].	21

Figure 2.6	Configuration of high resolution X-ray diffractometer [44].	22
Figure 2.7	Schematics of the Hall measurement [46].	23
Figure 2.8	Van der Pauw contact placement configurations [46].	24
Figure 2.9	Schematic description of a SEM [48].	25
Figure 2.10	Schematic for a typical AFM instrument [46].	26
Figure 2.11	Patterning using a) positive and b) negative photoresist [23].	28
Figure 2.12	The configuration of mask aligner system [49].	29
Figure 2.13	The configuration of inductively coupled plasma-reactive ion etching (ICP-RIE) system [56].	31
Figure 2.14	Configuration of the electron beam evaporator system.	31
Figure 2.15	Lift-off procedure for substrates masked with a) optical lithography and b) e-beam lithography.	32
Figure 2.16	Schematic illustration of PECVD system [59].	33
Figure 2.17	Top and cross-section view of TLM patterns.	34
Figure 2.18	Schematic description of the DC characterization setup.	35
Figure 2.19	A typical output characteristic of HEMT devices.	36
Figure 3.1	Cross sectional schematic of highly resistive GaN buffer structures	38
Figure 3.2	Cross sectional schematic of full HEMT structures.	41
Figure 3.3	Schematic illustration of fabrication steps.	42
Figure 3.4	Optical microscope image of mesa structures of the the fabricated HEMT devices.	43

Figure 3.5 Optical microscope images of ohmic contacts (a) before and (b) after annealing.	44
Figure 3.6 (a) Optical microscope and (b), (c) SEM images of gate electrodes.	45
Figure 3.7 Optical microscope image of 1st level metallization.	46
Figure 3.8 Optical microscope image of the sample following Si_3N_4 passivation.	46
Figure 3.9 Optical microscope image of the sample after Si_3N_4 passivation opening step.	47
Figure 3.10 Optical microscope images of (a) bridge posts and (b) close-view of bridge posts.	47
Figure 3.11 SEM images of air-bridges.	48
Figure 3.12 Optical microscope images of the finalized devices.	49
Figure 4.1 Reflectance transients for highly resistive GaN layers on SiC substrate.	52
Figure 4.2 A cross-sectional SEM image of highly resistive GaN layers.	53
Figure 4.3 AFM images of samples (a) A, (b) B, and (c) C.	54
Figure 4.4 The XRD $\omega/2\theta$ scans of the HR GaN structures.	55
Figure 4.5 Reflectance transients of HEMT control sample.	58
Figure 4.6 Reflectance transients of samples H1, H2 and H3.	59
Figure 4.7 HRXRD Rocking Curves for HEMT structures.	60
Figure 4.8 FWHM of AlGaN(002) ω scan of HEMT samples as a function of Al content of AlGaN.	61

Figure 4.9 Sheet carrier density and 2DEG mobility of HEMT samples as a function of Al content of AlGa _N	62
Figure 4.10 TLM data measured by four point probe method for sample H1.	63
Figure 4.11 TLM data measured by four point probe method for sample H2.	64
Figure 4.12 SEM image of the gate metal.	64
Figure 4.13 DC output characteristic of sample H1 and H2.	65
Figure 4.14 DC transfer characteristics of sample H1 and H2.	66
Figure 4.15 Breakdown voltage characteristics of sample H1 and H2.	66

LIST OF ABBREVIATIONS

LED	Light Emitting Diode
LD	Laser Diode
Wz	Wurtzite
ZB	Zinblende
MOCVD	Metal Organic Chemical Vapor Deposition
HEMT	High Electron Mobility Transistor
FET	Field Effect Transistor
JFET	Junction Field Effect Transistor
MESFET	Metal Semiconductor Field Effect Transistor
MOSFET	Metal Oxide Semiconductor Field Effect Transistor
MODFET	Modulation Doped Field Effect Transistor
2DEG	Two Dimensional Electron Gas
HRXRD	High Resolution X-ray Diffraction
SEM	Scanning Electron Microscopy
AFM	Atomic Force Microscopy
SI	Semi Insulating
IPA	Isopropanol
DI	Deionized
UV	Ultraviolet
EBL	Electron Beam Lithography
RIE	Reactive Ion Etching
ICP	Inductively Coupled Plasma
RTA	Rapid Thermal Annealing
RTP	Rapid Thermal Processing
PECVD	Plasma Enhanced Chemical Vapour Deposition
TLM	Transmission Line Model
DC	Direct Current
LT	Low Temperature
HT	High Temperature
NL	Nucleation Layer
2D	Two Dimensional
3D	Three Dimensional

CHAPTER 1

INTRODUCTION

III-nitrides are promising candidates that matured over the last few years for a wide variety of applications. This family primarily includes gallium nitride (GaN) and related alloys taking advantage over conventional semiconductors such as Si, GaAs and InP because of their direct and wide bandgap ranging from 1.9 eV to 6.2 eV (see Figure 1.1).

This difference in their bandgap and the strength between their bonds provide

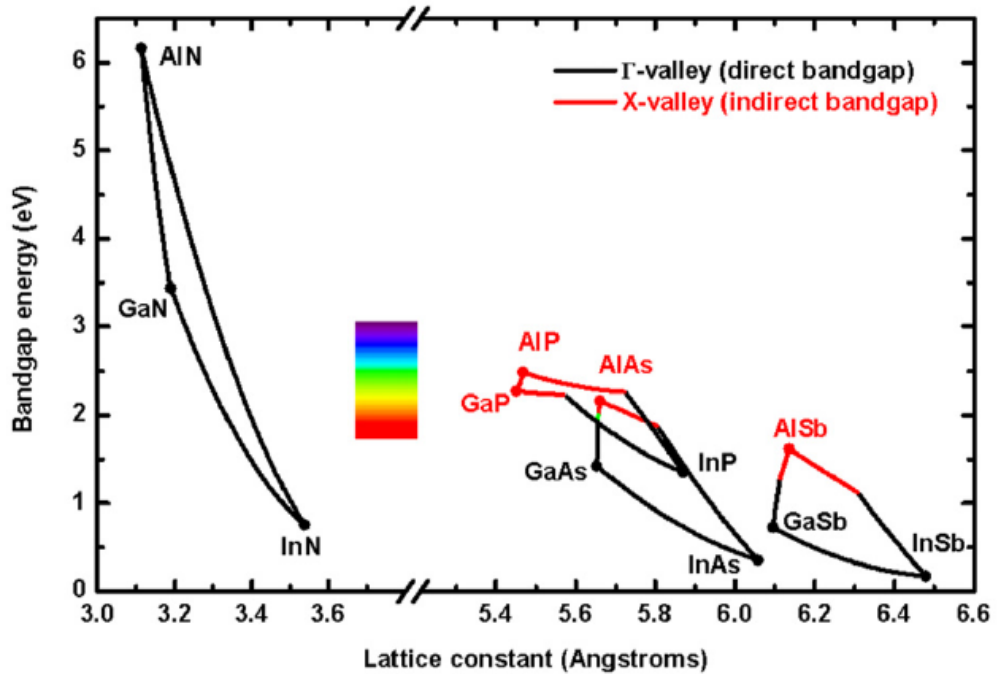


Figure 1.1: Bandgap energy vs lattice constant of III-V semiconductors at 300K [1].

Table 1.1: Electrical Properties of Semiconductors [2].

Material	Mobility $\mu(\text{cm}^2/\text{V.s})$	Dielectric Constant (ϵ)	Bandgap $E_g(\text{eV})$	Breakdown Field $E_b(10^6\text{V}/\text{cm})$	T_{max} ($^{\circ}\text{C}$)
Si	1300	11.90	1.12	0.30	300
GaAs	5000	12.50	1.42	0.40	300
4H-SiC	260	10.00	3.20	3.50	600
GaN	1500	9.50	3.40	2.00	700

these materials with superior properties for a wide spectrum of devices from high power, high temperature, high frequency electronic devices to optoelectronic devices such as light emitting diodes (LEDs) and laser diodes (LDs). Electrical properties of GaN in comparison to other wide band gap materials are shown in Table1.1 and application areas of GaN transistors are picturally shown in Figure1.2.

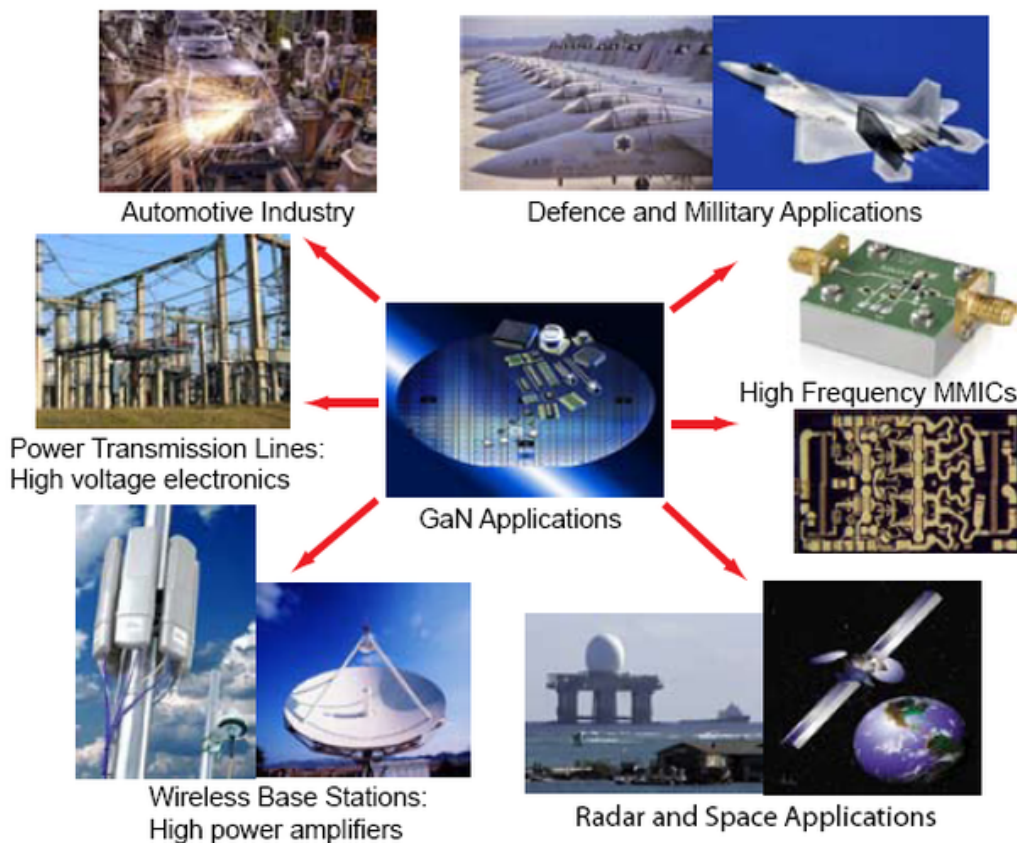


Figure 1.2: Application areas of GaN transistors [3].

GaN based transistors are ideal for both high power and high frequency electronics since they possess high saturation velocity, high breakdown fields, low specific on resistance, high current rating, fast switching time and the ability to form high quality AlGaN/GaN structures with excellent transport properties [4, 5].

Sapphire (Al_2O_3), silicon (Si), silicon carbide (SiC) or GaN itself are used as substrates for GaN growth. Since GaN substrates are available at very high prices, GaN is still commonly grown heteroepitaxially on lattice mismatched substrates. Once 4H-SiC or 6H-SiC substrates become commercially available, they took the place of sapphire and silicon due to their superior high power performance and thermal management [6].

1.1 Basic Properties of III-Nitride Materials

Compound semiconductors include group III-nitrides, GaN, indium nitride (InN), aluminium nitride (AlN) and their ternary and also quaternary alloys. They can be found in three different structures, which are wurtzite (Wz), zincblende (ZB) and rocksalt. Traditional semiconductors such as GaAs and InP have a zincblende structure. Thermodynamically stable phase is wurtzite for bulk GaN, AlN and InN for which no phase change or decomposition will occur once it is formed. The wurtzite structure has a hexagonal unit cell with two lattice parameters (length a and height c), which includes 6 atoms of each type. Lattice constants of group III-nitrides are provided in Table 1.2.

Each type of atom consist of two sublattices in the form of hexagonal closed packed (HCP), offset along the c -axis by $5/8$ of the cell height ($5c/8$), as shown in Figure 1.3.

The difference between wurtzite and zincblende structure is the stacking se-

Table 1.2: Lattice constants of group III-nitrides.

Properties	GaN	AlN	InN
a lattice constant (\AA)	3,19	3,11	3,83
c lattice constant (\AA)	5,19	4,98	5,69

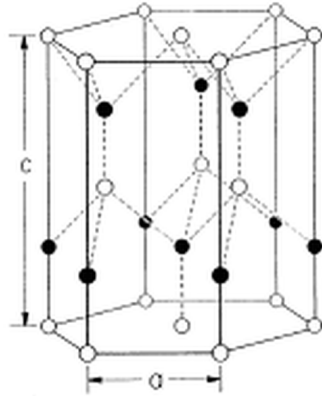


Figure 1.3: Hexagonal structure of wurtzite crystal.

quence of Group III and N pairs; in the wurtzite (0001) plane is stacked as ABABAB in $\langle 0001 \rangle$ direction; whereas in the zincblende (111) plane is stacked as ABCABC in the $\langle 111 \rangle$ direction. A stick and ball representation of both wurtzite and zincblende structures are shown in Figure 1.4. The difference between them is the bond angle of the second nearest neighbours.

The hexagonal bilayers are formed by anions and cations. Lack of inversion symmetry caused either group III element (Ga, Al, In) polarity or N polarity, which is referred as Ga-face or N-face crystal (as shown in Figure 1.5). The crystal orientation is determined by the substrate or might be changed by varying

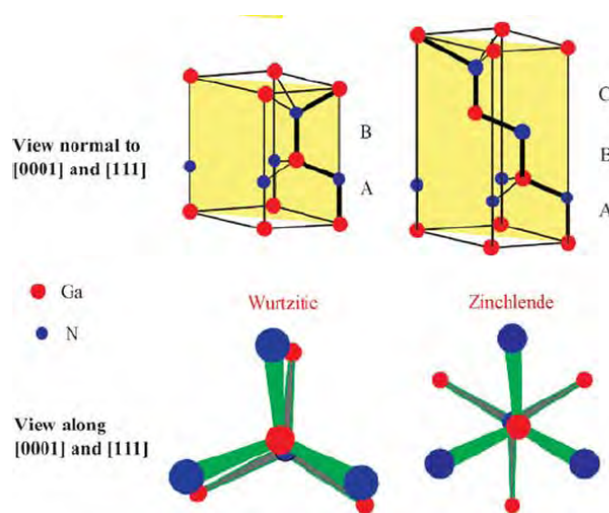


Figure 1.4: Stick and ball stacking model of wurtzite and zincblende crystals [7].

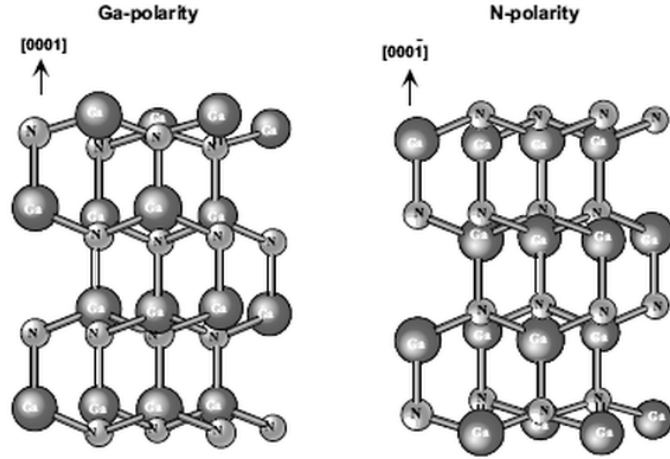


Figure 1.5: Different polarities of wurtzite GaN.

the growth techniques and substrates. GaN grown by MOCVD reactors on c-plane SiC or sapphire (Al_2O_3) substrates results in crystals with Ga-face [8].

1.2 AlGaN/GaN heterostructures

Most of the GaN based devices are made up of heterostructures containing two or more semiconductors with different bandgap E_g , permittivities ϵ , work functions ϕ and electron affinities χ . The ternary alloys of wurtzite polytypes of GaN and AlN form a continuous alloy system with a wide range of bandgaps and a small change in the lattice constants. The properties depend on the composition of the alloys.

When a narrow bandgap semiconductor is put into contact with a wide bandgap semiconductor layer, in case of thermal equilibrium the fermi level (E_F) of the semiconductors equilibrate resulting in a discontinuity in the conduction (E_c) and valence (E_v) band. When the wide bandgap semiconductor is n -doped, the ionized donors in the semiconductor compensate the accumulated negative charge. A strong localization occur perpendicular to the interface direction; thus, a triangular quantum well is formed between these two semiconductors. Parallel to the heterojunction, near the boundary at the bottom, electrons can

move freely and a two dimensional electron gas (2DEG) is formed as shown in Fig. 1.6 [9].

Since the narrow bandgap material is undoped and these electrons are away from the interface and since the electrons are separated from their donor atoms, this results in the reduction of Coulomb scattering. High saturation velocities and high electron mobilities can thus be achieved within the channel.

For the conventional III-V semiconductors such as GaAs, a doped layer is necessary for the formation of the 2DEG. On the contrary, for AlGaN/GaN heterostructures, existence of the polarization fields creates 2DEG with a very high electron concentration. Two types of polarization fields are present as spontaneous and piezoelectric polarizations, with polarization coefficients of P_{SP} and P_{PE} , respectively. The coefficients of III-N materials are mostly larger than that of conventional III-V semiconductors. Spontaneous polarization is the built-in polarization in the unstrained crystal since the bond between two atoms is not purely covalent and there is a lack of inversion symmetry. Compressively strained AlGaN layers are grown due to the lattice constant differences between GaN and AlN, where the piezoelectric polarization is created. The collection of the charge in the quantum well in AlGaN/GaN occurs due to the polarizations in both GaN and AlGaN layers. GaN layer has spontaneous polarization, whereas strained AlGaN layer has both spontaneous and piezoelectric polar-

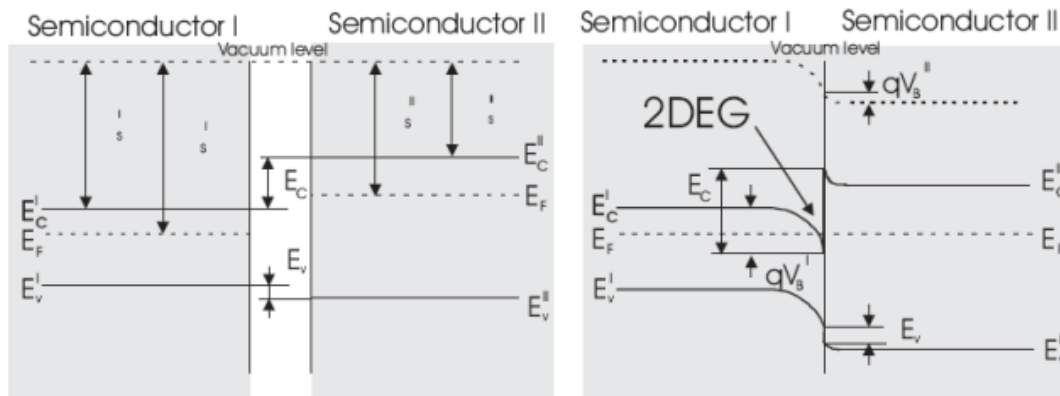


Figure 1.6: Band diagram of the heterostructure formed by wide (I) and narrow (II) bandgap semiconductors at thermodynamic equilibrium [10].

ization. The total polarization in AlGa_N layer is the sum of the spontaneous polarization and piezoelectric polarization. If this total polarization is greater than that of GaN buffer layer, polarization induced sheet charge is positive at lower AlGa_N/GaN interface for Ga-face structure. The free electrons tend to balance positive charge forms a 2DEG in the triangular quantum well. For N-face structure, polarization induced sheet charge is negative and compensated by holes present in the upper AlGa_N/GaN interface as depicted in Figure 1.7.

The sheet carrier concentrations of 10^{13} cm⁻² and mobility values of 2000 cm²/V.s at 300 K are obtained in 2DEG for similar structures. This makes AlGa_N/GaN heterostructures very attractive for applications in high frequency and high power electronic devices [7, 8].

1.2.1 High Electron Mobility Transistor (HEMT)

The earliest foundation of field effect transistors (FETs) dated back to middle thirties. FET basically consists of a semiconductor channel and two electrodes as drain and source at the ends. Gate, which is a control electrode is placed close

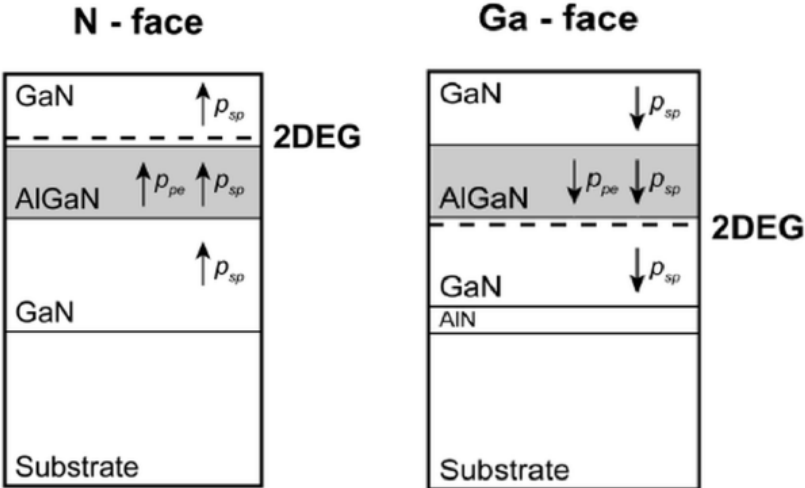


Figure 1.7: Polarization induced sheet charge density in AlGa_N/GaN heterostructure with N-face and Ga-face polarity.

to the channel to control the flow of carriers (electrons or holes) from source to drain. The semiconductor can be either n -type or p -type. The most basic type of FET is junction field effect transistor (JFET), which uses a reverse biased diode junction. In 1947, William Shockley and his colleagues at Bell laboratories observed modulation of current flowing in a semiconductor channel. Later in 1960, metal oxide semiconductor field effect transistor (MOSFET) was invented by Dawon Kahng and Martin Atalla based on Shockley's original field effect theories [11]. MOSFET is a different type of FET, which has an insulated gate different from metal semiconductor field effect transistor (MESFETs). A thin oxide layer is generally used between gate electrode and the channel in MOSFETs. In the late seventies, working mechanism of quantum well structures with the idea of modulation doping received great attention [12]. Takashi Mimura and his team were conducting research on gallium arsenide (GaAs) MOSFETs, the first attempt was unsuccessful since the electrons were encapsulated by high density of the surface states near the interface. This problem was overcome by modulation of the width of depletion region leading to the discovery of depletion-type MOSFETs. Further investigations came up with the idea of using a field effect from a Schottky gate contact to control the electrons at the interface. Thus, the first AlGaAs/GaAs HEMTs were reported [13, 14]. In the early eighties, HEMT structures were become more and more popular and started to receive great attention after the HEMT devices were published as the semiconductor devices with the lowest noise characteristics in the world [15]. The main difference between HEMTs and MOSFETs or MESFETs is that, it uses a specialized PN junction which is a heterojunction consists of two materials with different bandgaps. The most commonly used materials are AlGaAs/GaAs for this purpose advantages of HEMTs over MOSFETs include high electron mobility, small source resistance, high electron velocity in large electric fields, high gain bandwidth, high transconductance due to small gate-channel distance, high output resistance and higher Schottky barrier height [16].

Deposition of high quality GaN films on sapphire was demonstrated despite the problems of high n -type background carrier concentration, difficulty of p -type doping and unavailability of GaN substrate. Using two-step growth process

able to improve the structural and electrical properties [17]. In 1980s, different methods including MOCVD were developed to grow GaN on sapphire substrates. Subsequently, Khan demonstrated the first AlGaN/GaN HEMT in 1994 [18, 19, 20]. The superior properties of GaN such as wide bandgap, high breakdown voltage and high operation temperature and the polarization effect of AlGaN/GaN structures result in a high electron sheet charge density which shifts the main interest from AlGaAs/GaAs to AlGaN/GaN devices [21]. Typical $\text{Al}_x\text{Ga}_{(1-x)}\text{N}/\text{GaN}$ HEMT structure is schematically provided in Figure 1.8. HEMT, also called as modulation doped field effect transistor (MODFET) operates on the basis of charge accumulation. HEMT similar to other FETs, is a three terminal device containing source, drain and gate contacts as shown in Figure 1.8. The current between source and drain can be controlled by the gate voltage and flows through the two dimensional conducting channel formed by 2DEG. If gate voltage is increased more towards to negative values (threshold voltage, V_{th}), 2DEG region is depleted under gate and the flow of current between source and drain is decreased until the channel is pinched-off. This AlGaN/GaN HEMT operates in depletion mode (normally on). When the threshold voltage is adjusted to be positive values, HEMT operates in the enhancement mode (normally off). Changing the mode of operation depends on both epitaxial structure and fabrication technique [22]. Typical layers from top the bottom are as follows:

Cap Layer: To reduce the gate leakage, increase the ohmic contact resistance

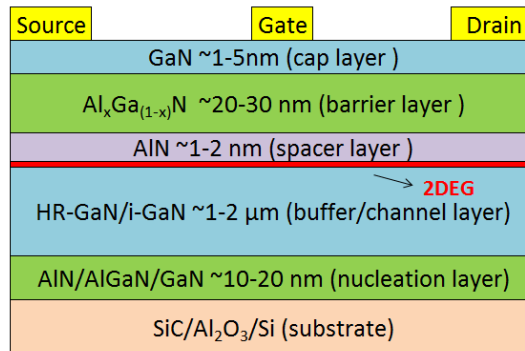


Figure 1.8: Schematic HEMT structure.

and increase the Schottky barrier height a thin ($\sim 1-5$ nm) cap layer is deposited on top of the barrier layer. It also prevents surface from oxidation. GaN cap layer is used in this study [3, 23].

Barrier Layer: The most crucial layer of the HEMT structure is the barrier layer. It is the wider bandgap material forming the 2DEG at the channel interface. AlGa_xN layer is used in this study. Al mole fraction (x) determines the bandgap of Al_xGa_(1-x)N layer. Size of the bandgap is determined by the following equation:

$$E_g(x) = xE_g(\text{AlN}) + (1 - x)E_g(\text{GaN}) - bx(1 - x) \quad (1.1)$$

,where b is the bowing parameter. Various bowing parameter values from -0.8 eV (upward bowing) to +2.6 eV (downward bowing) are reported in the literature [24].

Thickness and Al fraction affects the 2DEG properties. Increasing Al mole fraction up to a certain level results in an increase in the 2DEG sheet carrier concentration. In addition, the thickness should be above a critical thickness on the other hand it should be below where the relaxation occurs [7, 25].

Spacer Layer: A very thin spacer aluminium nitride (AlN) ($\sim 1-2$ nm) layer is placed between buffer and barrier layers, to increase the sheet carrier concentration through the elimination of alloy disorder scattering and the reduction of interface roughness scattering. Moreover, the spacer layer decreases the Coulomb scattering between 2DEG electrons and their ionized parent atoms in the supply layer resulting in an increase in the 2DEG mobility [26, 27, 28].

Buffer/Channel Layer: This layer consists of a material with a lower bandgap than barrier layer. Highly resistive GaN or semi-insulating GaN can be used for this purpose. This layer should have low defect density and a smooth surface. Besides, it determines the properties of HEMT device such as buffer leakage, drain current collapse, output power reduction, pinch-off voltage and breakdown voltage values. In this thesis, highly resistive GaN layer is used as a buffer layer. Thickness of this layer should be high ($\sim 1-2$ μm) to achieve a good 2DEG mobility and sheet carrier concentration [29, 30].

Nucleation Layer: Nucleation layer (NL) depends on the choice of the substrate. Very thin AlN, AlGa_N or GaN layers can be used. Generally, low temperature GaN or two step AlN layers are used for SiC substrates. Nucleation layer acts as a template between GaN buffer layer and SiC substrate releasing strain due to the lattice mismatch in between. There are different routes for the deposition of nucleation layers. In this study, a thin nucleation layer (NL) of AlN is deposited at low temperature (LT) then this layer is annealed. Subsequently, AlN layer at high temperature (HT) is deposited. Nucleation layer decreases the threading dislocation density within the GaN buffer layer. [31]

Substrate GaN, SiC, Al₂O₃ and Si can be used as epitaxial substrates for the deposition of GaN. 6H-SiC is preferred in this study due to the small lattice mismatch and its high thermal conductivity. A detailed analysis of the substrates will be provided in Chapter 2.

In order to obtain devices with high performance for both high power and high frequency applications, following parameters must be adjusted accordingly:

- Buffer leakage; highly resistive buffer layers with low leakage and low defect density.
- Breakdown voltage (V_{BR}); high quality material, proper surface passivation, low buffer leakage.
- Sheet charge density (n_s); high Al concentration without strain relaxation to maximize the polarizations (both P_{SE} and P_{PE}).
- Electron velocity (ν); reducing effective gate length (L_g) and gate length extension.
- Electron mobility (μ); reducing of scattering centers due to dislocations, interface roughness and alloy disordering at the heterojunction.
- Thermal conductivity; proper substrate to remove the generated heat during operation.
- Minimizing short-channel effect.

- Conductivity; maximizing $n_s \times \mu$ product. Conductivity of 2DEG is given by the equation:

$$\sigma = qn_s\mu \quad (1.2)$$

, where q is electron charge, n_s is the sheet carrier concentration of free electrons and μ is the mobility of the electrons.

Highly resistive or semi-insulating GaN buffer layer is necessary to obtain HEMT device with a good performance. Typically unintentionally doped GaN grown by MOCVD shows n -type conductivity due to the residual donors. These residual donors have to be compensated to achieve highly resistive or semi-insulating GaN. Widely used method for this purpose is creating deep acceptor states by intentional doping the GaN layers with Iron (Fe), Chromium (Cr) and Carbon (C). The other approach is introducing dislocations or carbon impurities to achieve highly resistive GaN buffer layer [32, 33, 34]. In this thesis, the motivation is using the second approach by adjusting the growth parameters without degrading the crystal quality, surface morphology, 2DEG properties and device performance.

CHAPTER 2

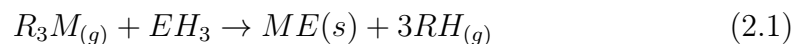
MOCVD GROWTH AND FABRICATION OF HEMT DEVICES

In this Chapter, epitaxial growth of HEMT structures and issues regarding the fabrication of devices will be discussed. In the first part, metalorganic chemical vapor deposition (MOCVD) method and the growth system will be explained in detail. Detailed materials characterization via in-situ reflectometry, high resolution X-Ray diffraction (HRXRD), Hall Effect measurements, scanning electron microscopy (SEM) and atomic force microscopy (AFM) will be discussed. Afterwards, fabrication steps of HEMT devices and device characteristics (direct current (DC) characterization) will be presented.

2.1 Metalorganic Chemical Vapor Deposition (MOCVD)

MOCVD is a specialized type of chemical vapor deposition used for the epitaxial growth of semiconductors on substrates. It is the most commonly used process for the deposition of nitride layers; especially for GaN and derivatives. The high quality and high purity of epitaxial layers deposited through MOCVD method are used for a variety of electronic applications including HEMTs.

MOCVD utilizes vapor transport of the precursor molecules and their subsequent reactions towards the heated substrate. The precursors are group III alkyls and group V hydrides for III-nitride epitaxial films. A general pyrolysis reaction can be written as:



,where R_3M and EH_3 are denoted as group III alkyls and group V hydrides, respectively, and R is an organic radical, M is an organic metal from group III and E is a nonmetal from Group V.

High quality epitaxial layers should have low defect density and impurity levels and should not possess abrupt interfaces and sharp transitions in composition, which are directly related to the nature and purity of the precursors. Intrinsic impurities (e.g. carbon) are affected by the thermal stability and chemical nature of the bonds in the precursor molecules, whereas extrinsic impurities (e.g. Si, Mg, O, etc.) are determined by the synthesis and purification methods [35]. A suitable precursor should have following properties:

- should be stable at room temperature,
- should have a high purity,
- should not decompose under storage conditions,
- should not be influenced by early decomposition reactions while transported via carrier gases (nitrogen (N_2) or hydrogen (H_2)),
- should decompose very cleanly and easily at the required vaporization temperatures without incorporation of residual carbons,
- should have low toxicity.

Precursors for the deposition of III-V materials or for n/p -type doping are listed in Table 2.1. Generally, following precursors are used for the GaN epitaxial growths: Trimethylgallium (TMGa) for Ga, trimethylaluminium (TMAI) for Al, trimethylindium (TMIIn) for In and ammonia(NH_3) for N. For the group III-V based compounds chemical reactions for GaN, AlN and AlGaN are as follows:

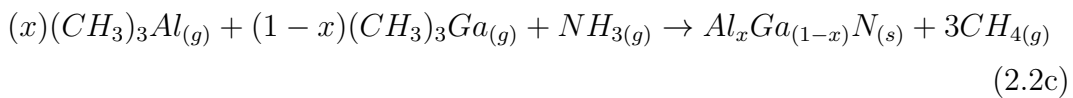


Table 2.1: Precursors for MOCVD [36].

Name of Compound	Acronym	Purpose
Trimethylgallium	TMGa	III element
Triethylgallium	TEGa	III element
Trimethylaluminium	TMAI	III element
Triethylaluminium	TEAl	III element
Trimethylindium	TMIIn	III element
Triethylindium	TeIn	III element
Ethyldimethylindium	EDMIIn	III element
Trimethylantimony	TMSb	V element
Triethylantimony	TESb	V element
Trimethylarsine	TMAAs	V element
Dimethylarsinehydride	DEAs	V element
tert-Butylarsine	TBAs	V element
tert-Butylphosphine	TBP	V element
Arshine	AsH ₃	V element
Phosphine	PH ₃	V element
Ammonium	NH ₃	V element
Hydrogen Selenide	H ₂ Se	n dopant
Hydrogen Sulfide	H ₂ S	n dopant
Silane	SiH ₄	n dopant
Disilane	Si ₂ H ₆	n dopant
Tetramethyltin	TMSn	n dopant
Tetraethyltin	TESn	n dopant
Dimethylzinc	DMZn	p dopant
Diethylzinc	DEZn	p dopant
Diethylberyllium	DEBe	p dopant
Dimethylcadmium	DMCd	p dopant
Bis-cyclopentadienyl magnesium	BCp ₂ Mg	p dopant

During MOCVD, the precursor molecules are transported by the carrier gas either nitrogen (N₂) or hydrogen (H₂), to the heated susceptor, where the gas phase reactions take place. Two growth regimes can be achieved, which are either kinetically or diffusion controlled. The resulting species diffuse towards the growing surface which would then get adsorbed onto the surface. They can decompose or desorb, then diffuse through for the final incorporation reactions. Products form new bonds with the substrate resulting in the deposition of a semiconducting thin film. The resulting by-products are evaporated into the

chamber and carried away through the reactor exhaust. Schematic representation of the MOCVD process is provided in Figure 2.1 [31, 36].

2.1.1 Setup of MOCVD System

MOCVD system consists of a gas handling system, vacuum and exhaust system, a reactor, a heating system, a command unit (computer) and a safety system. The growth occurs in a horizontal reactor that can operate at pressures from 100 to 1000 mbar. In the horizontal reactor there are quartz parts which contain an inductively heated (through radio frequency (RF) coils) graphite susceptor. Temperatures up to 1200°C can be achieved within this system. A single 2 inch wafer can be placed onto a rotating susceptor. Rotation of the susceptor achieved by gas foil rotation using N₂ or H₂ gases, provides the growth of uniform layers.

The gas handling system includes the metalorganic sources of alkyls and hydrides, pumps, valves and gas flow controllers. The precursors are mixed with carrier gas and transported into the reactor. Stainless-steel tubes are used for transportation. Gas lines have to be leak tight and clean to achieve deposition of

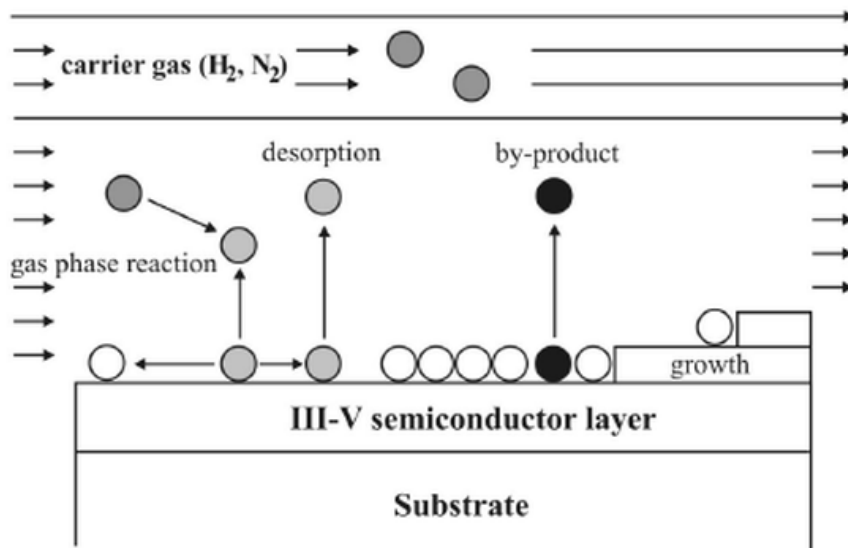


Figure 2.1: The principle of MOCVD process [7].

high purity and high quality layers. Group III precursors (either liquid or solid) are stored in bubblers whose temperature is controlled by thermal bath systems. Electronic mass flow controllers are attached to them to allow controlled supply of the precursor and carrier gas into the reactor. Group V precursors are compressed gases, so they are stored in the cylinders. Group III and group V precursors are transported to the reactor via two separate lines, which are denoted as run MO and run hydride lines, to prevent the reactions in between before they to reach the reactor. A third line, called vent line, directly transports gas to the exhaust. Both run and hydride lines are pressure controlled before reaching the reactor. Gases mix near the susceptor and inside the reactor. This eliminates the pressure variations while switching the gases. At the end of the reactions, remnants are carried away through the reactor exhaust line. Within the exhaust line, the poisonous by-products are chemically treated at the scrubber. A schematic setup of the system and the reactor is provided in Figure 2.2. The pressures, growth parameters are adjusted and mass flow controllers and valves are controlled through PLC (programmable logic controller) computer. The heating is accomplished by inductive radio frequency coils placed at the

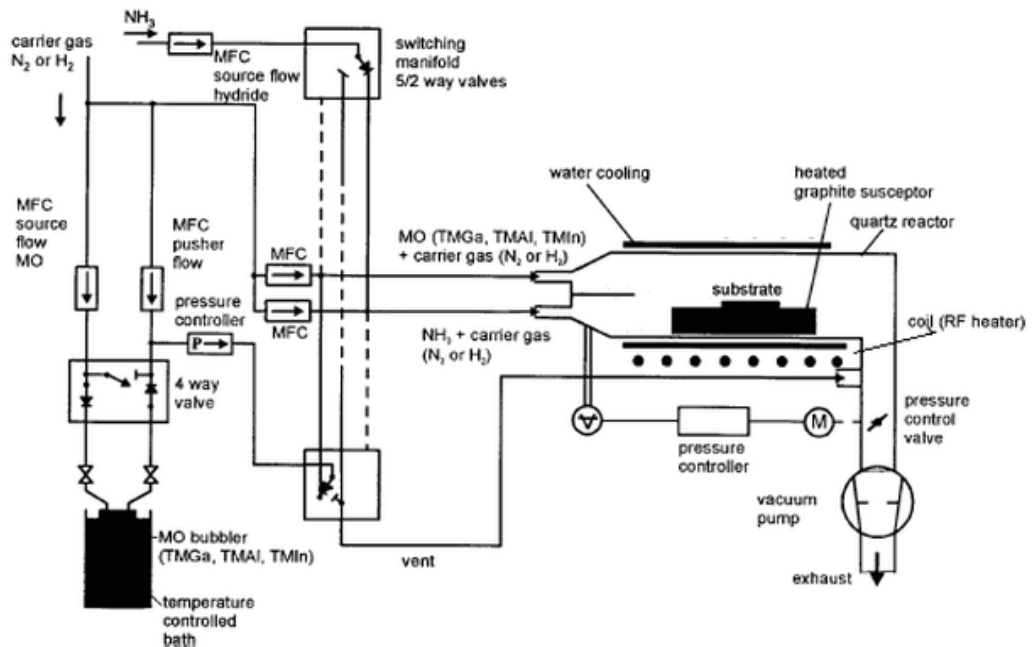


Figure 2.2: Schematic of the reactor [37].

bottom of the reactor under the susceptor. To prevent the contamination of the reactor, a nitrogen purged glovebox is used for substrate loading and unloading.

2.1.2 Choice of Substrate

The choice of the substrate is primarily depend on the application. Theoretically GaN itself is the best substrate for III-nitride epitaxy; but, because of its high price, heteroepitaxial and mismatched substrates are preferred [38]. Crystal structure, reactivity, composition, surface finish, chemical, thermal and electrical properties of the substrates need to be considered for the application needs [7, 36]. Properties of the substrates that are available for the deposition of III-nitrides are presented in Table 2.2.

Through the development of HEMTs, sapphire (Al_2O_3) and SiC substrates come into use. Sapphire has lower thermal conductivity compared to SiC. In addition, electrical conductivity of SiC is higher than sapphire; however, it is problematic for RF devices. Although it is expensive compared to sapphire, following the commercial availability of semi insulating (SI) 4H or 6H-SiC substrates, its high thermal conductivity makes it the leading substrate for high power devices. It is manufactured in large quantities, where good quality wafers at a reasonable price can be obtained. It has low lattice and thermal expansion coefficient mismatch with GaN (3.5% and 30%, respectively). Because of the poor wetting between GaN and SiC, AlN or AlGaIn nucleation layers are used to improve wetting and decrease the number of dislocations. This improves lattice match between GaN and AlN [31].

Table 2.2: Properties of substrates that are available for III nitride epitaxy [39].

Substrate	AlN	GaN	Al_2O_3	SiC	Si
thermal conductivity (W/cm K)	3.3	1.3	0.5	3.0-3.8	1.0-1.5
lattice mismatch (%)	-2.4	-	-16	+3.5	-17
resistivity (%)	high	high	high	high	mediate
cost	high	high	low	high	low
wafer size (inch)	small	small	6	3	12

2.2 Material Characterization

Material characterization can be divided into two groups as in-situ monitoring during deposition and ex-situ characterizations following deposition (i.e. structural, morphological and electrical).

2.2.1 In-situ characterization

In-situ characterization of layers during epitaxial growth are made with optical reflectance measurements. They provide real-time information about the growth rate, layer thickness and surface roughness. Schematic description of configuration is provided in Figure 2.3. The reflectometer composed of a light source, filters, mirror and a beam splitter. The intensity of reflected light from the surface is measured at one single wavelength as a function of time. To measure the thickness and growth rate of the layer, period of the modulated intensity is used. Intensity modulation depends on the transparency of the growth layer to the incident light.

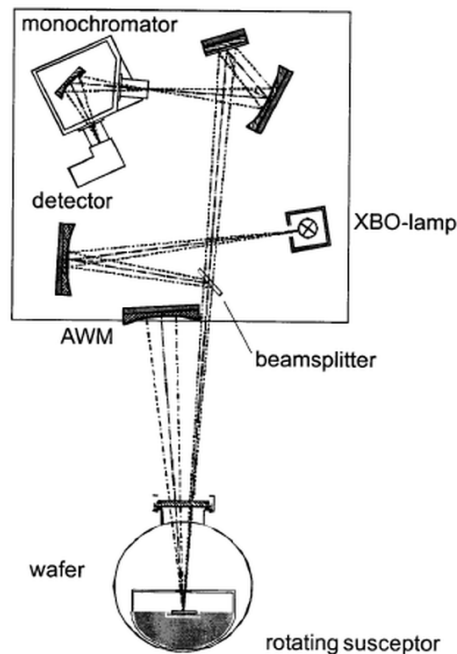


Figure 2.3: The configuration of in-situ characterization system [40].

Since there is a phase difference between incident and reflected light due to the layers with different refractive index as shown in Figure 2.4, constructive or destructive interference patterns will result in an intensity modulation of the reflected light. This is known as the Fabry-Perot oscillations. The superposition of reflected beams leads to the overall intensity. Using Fabry-Perot oscillations, the layer thickness and growth rates can be derived as follows:

$$nd = (m)\frac{\lambda}{2} \quad (2.3a)$$

$$\mu_{gr} = \frac{\lambda}{2n\Delta t} \quad (2.3b)$$

,where n is the refractive index, d is the thickness of the layer, m is the even number, λ is the wavelength of the light, μ_{gr} is the growth rate and Δt is the period of oscillations.

Short period in intensity modulation indicate high growth rates; whereas, long periods indicates low growth rates. Moreover, narrow bandgap semiconductors show shorter periodicity, while wide bandgap semiconductors yield longer periodicity. Compositional information can be derived from the changes of the amplitude (the maximum and minimum) of the reflectance transients. In addition, optical waviness of the reflectance transients indicate that there is a local fluctuation in layer thickness or refractive index during growth. Also, change in the composition because of the strain effects shows an increase in the roughness

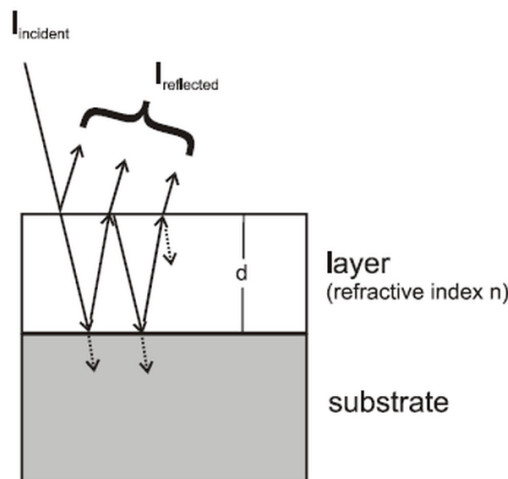


Figure 2.4: Reflection of light from a substrate-layer system [41].

of the transient signals [42, 41]. A typical example for reflectance transients measured at a wavelength 600 nm is provided in Figure 2.5.

2.2.2 Ex-situ layer characterization

In order to optimize growth parameters, ex-situ characterization techniques are applied in addition to in-situ characterization. Characterization techniques used in this work will be presented in detail in this section.

2.2.2.1 High Resolution X-Ray Diffraction (HRXRD)

X-Ray diffraction (XRD) is a widely used tool for the structural characterization of epitaxial layers. Various information about the crystal structure, composition of ternary compounds, layer orientation, lattice constants of epilayer, strain and dislocation density can be obtained from XRD. XRD analysis is based on the detection of X-Rays scattered from various crystallographic planes. Bragg's Law

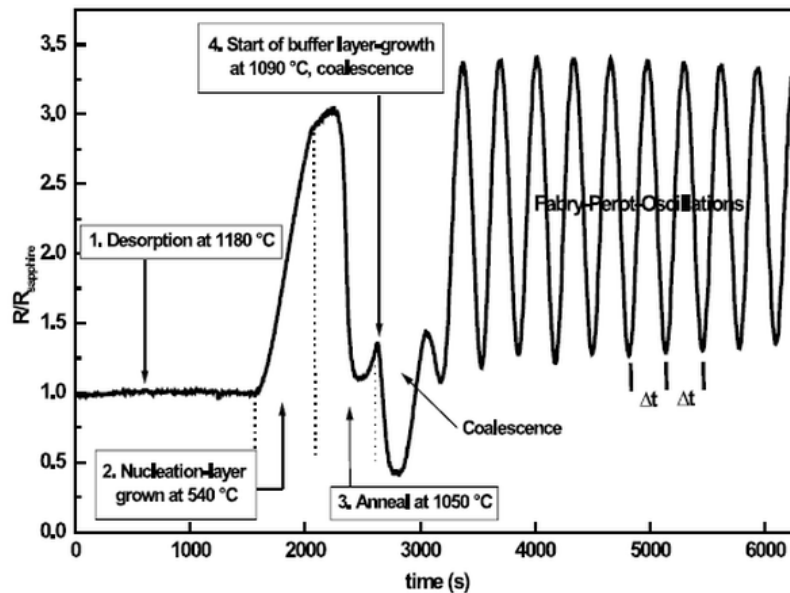


Figure 2.5: A typical reflectance transient [37].

is used to explain the diffraction condition:

$$n\lambda = 2d_{hkl}\sin\theta \quad (2.4)$$

,where n is the integer number describing the order of reflection, λ is the X-Ray wavelength, d_{hkl} is the spacing between the lattice planes and θ is the Bragg angle for which a maximum diffraction intensity occurs. The lattice spacing for a hexagonal crystal system is given by:

$$d_{hkl} = \frac{1}{\sqrt{\frac{4}{3}\left(\frac{h^2+hk+k^2}{a^2}\right) + \frac{l^2}{c^2}}} \quad (2.5)$$

,where a and c are lattice constants, hkl are Miller indices [43]. The XRD system composed of an X-Ray source, slits, a monochromator and a detector. Schematics of a diffractometer is shown in Figure 2.6. There are totally four rotating axes. θ , 2θ , Ψ , ϕ for different scan modes.

Two basic types of scans are; ω and $2\theta/\omega$. Once the detector is fixed at 2θ (twice Bragg angle) ω scans can be made. On the other hand, in $2\theta/\omega$ scans, both angles are set to the Bragg condition, where they are linked at a 1:2 ratio. Both symmetric and asymmetric Bragg reflections can be analysed. Lattice planes are parallel to the surface normal and Miller indices are $h=k=0$ (e.g.[002]) for symmetric rocking curves. On the contrary, asymmetric rocking curves have

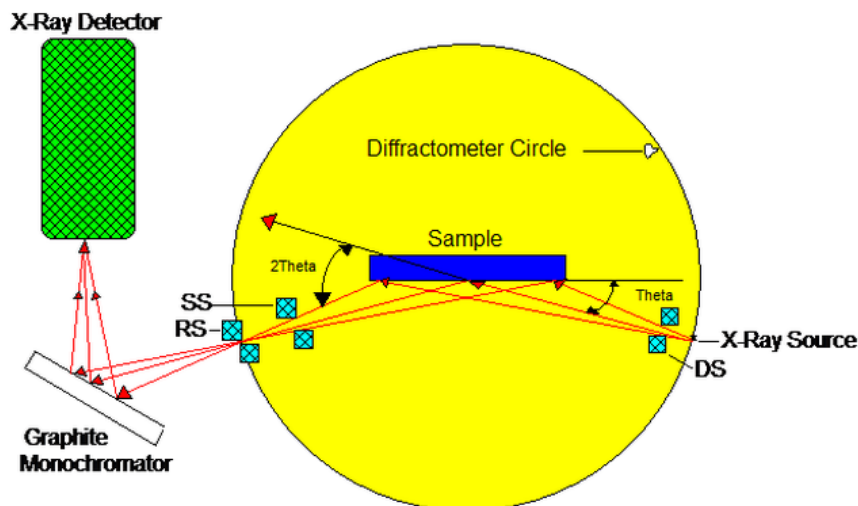


Figure 2.6: Configuration of high resolution X-ray diffractometer [44].

Miller indices $h, k \neq 0$, and the planes are not parallel to the surface normal. Crystal quality can be determined with HRXRD scans.

2.2.2.2 Hall Effect Measurements

Hall Effect measurements are used to determine electrical properties of materials such as mobility, carrier concentration and sheet resistance. The basic principle is the Lorentz force, where deflection of a moving electron occur under an applied magnetic field. If the current (I) is flowing through the sample and magnetic field (\mathbf{B}) is applied perpendicular to the current flow, then the Hall voltage V_H is induced perpendicular to both I and (\mathbf{B}) [45]. The principle is demonstrated schematically in Figure 2.7.

The Hall voltage is given by

$$V_H = \frac{IB}{nqd} IB \quad (2.6)$$

, where d is the thickness of the sample. Sheet carrier concentration is found by using $n_s = nd$ as

$$n_s = \frac{IB}{q|V_H|} \quad (2.7)$$

For convenience, Van Der Pauw method is used to find sheet resistance (R_s).

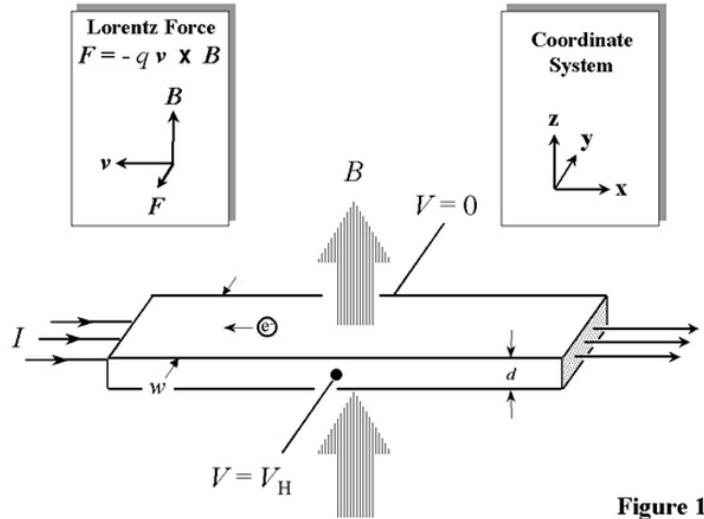


Figure 2.7: Schematics of the Hall measurement [46].

Four contacts on the periphery of an arbitrarily shaped sample is placed, a fixed current I through one pair of contacts is injected and measuring the V across the other pair of contacts can be measured. Consequently R_s can be calculated. Following conditions are required for the application of this method; the samples should be flat, should have uniform thickness and the contacts should be small at the edge of the samples. Different contact placements are depicted in Figure 2.8.

At first, I is applied through contacts 1-2 (I_{12}) and 2-3 (I_{23}) and voltage is measured between contacts 3-4 (V_{34}) and 4-1 (V_{41}); respectively. Using these values two characteristic resistances; $R_A = \frac{V_{34}}{I_{12}}$ and $R_B = \frac{V_{41}}{I_{23}}$ are calculated and the R_s related to these resistances is given by Van Der Pauw formula [47]:

$$e^{(-\pi \frac{R_A}{R_s})} + e^{(-\pi \frac{R_B}{R_s})} = 1 \quad (2.8)$$

and mobility (μ_n) is calculated from:

$$\mu_n = \frac{1}{en_s R_s} \quad (2.9)$$

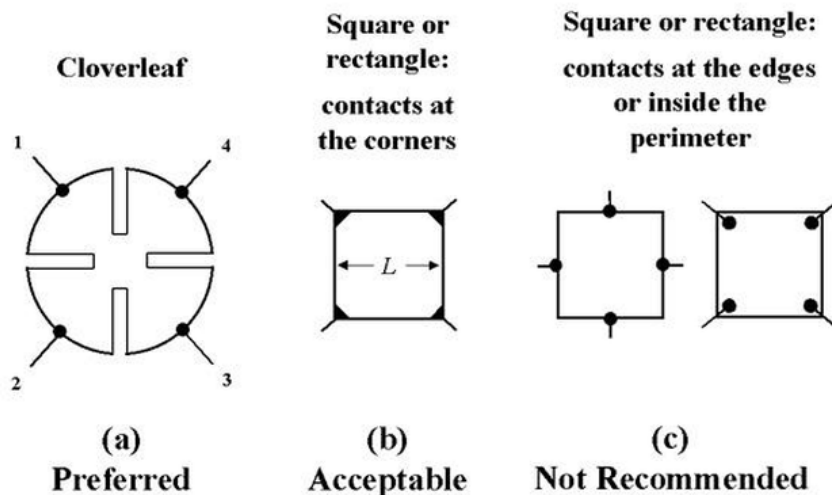


Figure 2.8: Van der Pauw contact placement configurations [46].

2.2.2.3 Scanning Electron Microscopy (SEM)

Scanning Electron Microscopy is used to obtain morphological and topographical information from surfaces. The SEM system consists of an electron gun, electromagnetic lenses, detector and vacuum equipments. Operating principle of SEM is as follows: An accelerated e-beam hit the (semi) conductive sample and generate secondary electrons that are detected by an electron detector. The electron beam (e-beam) is guided by the electromagnetic lenses. From the collected data an image can be obtained. This process occurs in a vacuum environment ranging from 10^{-4} to 10^{-10} Torr. The configuration of the system is presented in Figure 2.9.

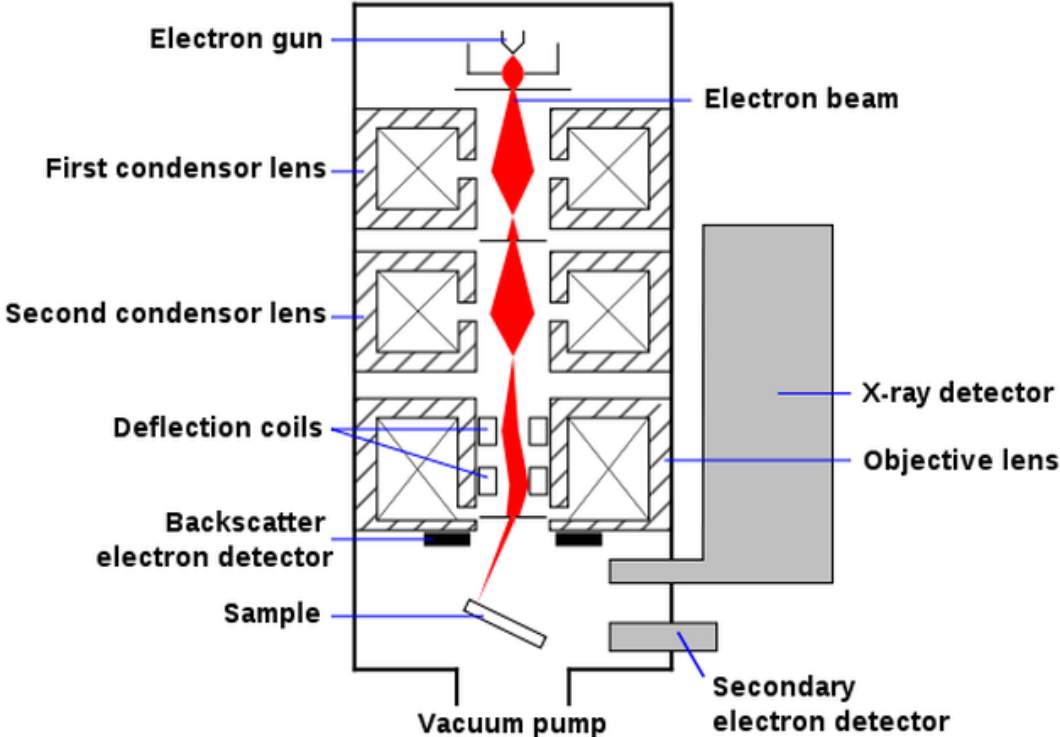


Figure 2.9: Schematic description of a SEM [48].

2.2.2.4 Atomic Force Microscopy (AFM)

Atomic force microscope allows three dimensional topographical imaging. It is used to analyse the sample surface in atomic scale resolution and calculate the surface roughness. In this technique, a sharp tip mounted on a flexible cantilever scans across the sample surface by a maintained constant force. The scanning motion is derived by a piezoelectric tube scanner. The tip-sample interaction is detected by the reflection of a focused laser beam on the back of the cantilever. Cantilever's deflection or oscillation amplitude changes are obtained through a photodetector simply by measuring the difference in output voltages. Systems can be operated in three different modes as contact, non-contact and tapping. In this work, contact mode is used, where the tip slightly touches the surface and deflection of the cantilever is detected via the position of the laser spot on the photodetector(Figure 2.10).

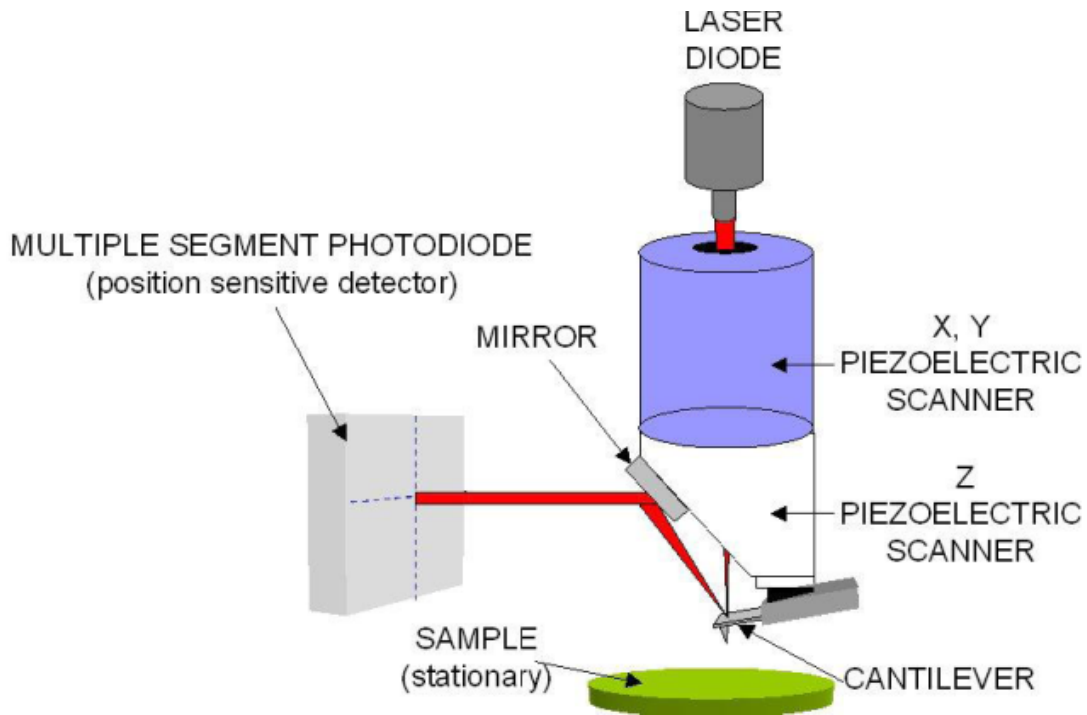


Figure 2.10: Schematic for a typical AFM instrument [46].

2.3 Device Processing

In this section, fabrication processes for the HEMT devices will be presented. The processing techniques include sample preparation, lithography, metallization, mesa isolation, annealing and passivation.

2.3.1 Wafer preparation

Fabrication starts with the preparation of the wafer samples. It is necessary to remove the native oxide coming from ambient and the residual photoresists from dicing. Standard cleaning procedure includes the sonication of the wafers in acetone followed by isopropanol (IPA) for several minutes. Wafers are then rinsed with deionized (DI) water and dried by blowing nitrogen (N_2).

2.3.2 Lithography

Lithography is the most basic step in the processing of any semiconductor device. Main aim is the transfer of the feature patterns from masks to a resist. Two alternative techniques are available, which are optical and e-beam lithography (EBL). Both photolithography and e-beam lithography is used in this work. E-beam lithography provides higher resolution and is used for the fabrication of submicron patterns.

2.3.2.1 Optical Lithography

Optical lithography necessitates ultraviolet (UV) light sensitive polymers called photoresists. The process steps right after substrate cleaning includes photoresist coating, soft baking, UV exposure, development and post baking. The removal of resists performed with a procedure called lift-off. Different types of resists can be used depending on the application. Resists can be divided into two categories as positive or negative. For positive photoresists, the exposed areas are removed during the development stage, whereas for negative ones regions

behind the masks are removed. The exact patterns in the mask are transferred to the substrate upon the use of positive photoresists. Whereas, reverse image is obtained upon the use of negative photoresist as shown in Figure 2.11. Positive photoresists are used for masking for etching processes and negative photoresists are used for metallization process.

A thin layer of photoresist is deposited onto the cleaned samples using spin coating. The thickness of the resist is determined by the spinning speed and time of the spin. A uniform resist layer is necessary for the good quality lithography. Right after, the sample is baked to remove the solvent from the resist and increase its adhesion to the substrate. The mask is then aligned using a mask aligner system. The configuration is presented in Figure 2.12. Aligned sample is exposed to the UV light for a certain amount of time depending on the type of the photoresist. Finally, the patterns are developed using proper developer.

For image reverse process, after first expose, samples are post-baked to cross link the polymer bonds in the exposed region. Then finally, the samples are exposed to the UV light without photomasks. Using this method, firstly masked

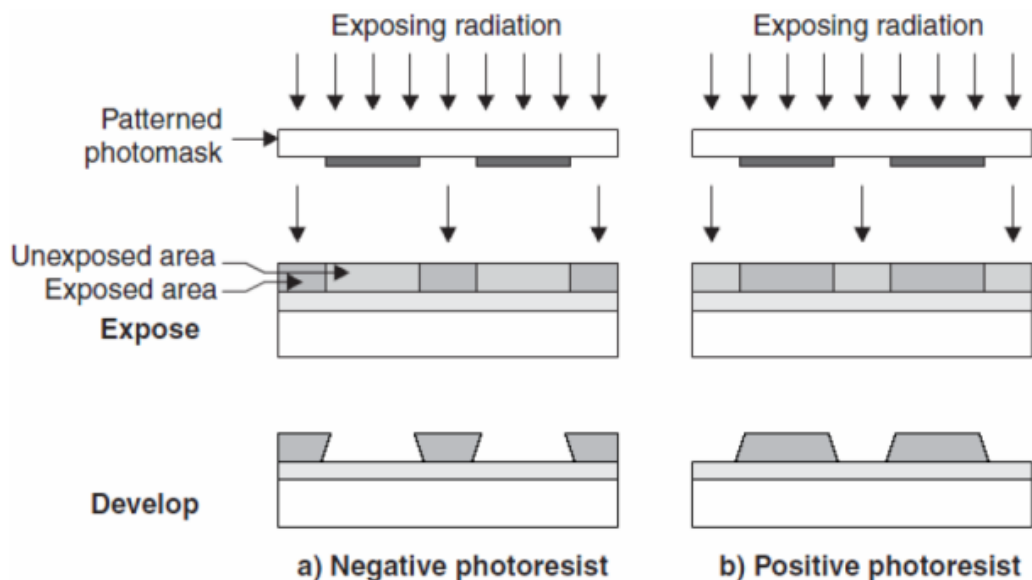


Figure 2.11: Patterning using a) positive and b) negative photoresist [23].

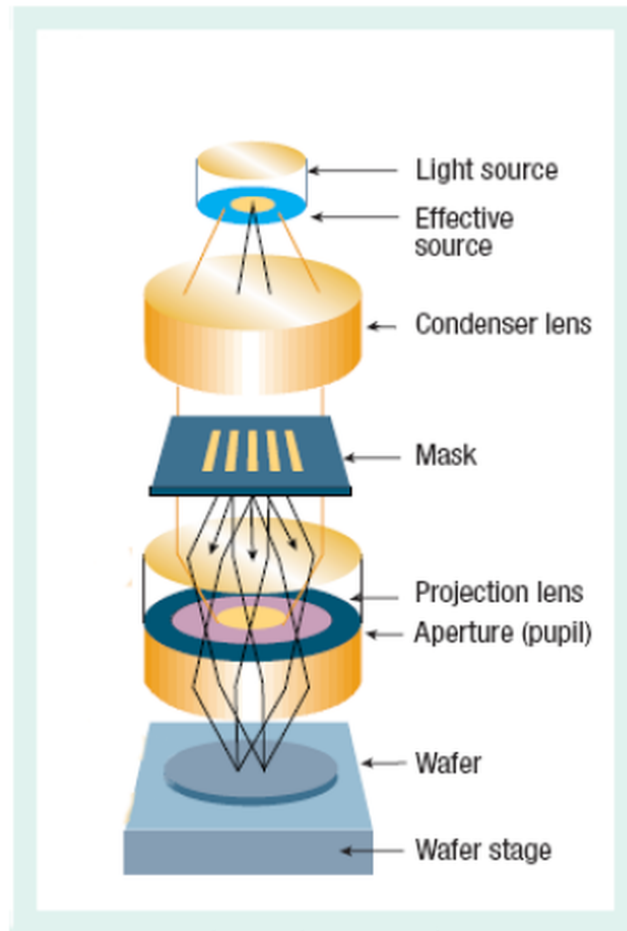


Figure 2.12: The configuration of mask aligner system [49].

regions was made soluble in the developer and a resist profile with undercuts are obtained that is appropriate for the lift-off procedure.

2.3.2.2 Electron Beam Lithography (EBL)

E-beam lithography (EBL) system consists of electron source, electron accelerator unit, e-beam focusing unit, beam deflection, pattern generator and stage translation units. EBL is used to create submicron patterns with high resolution and alignment accuracy. Special kinds of resists, which undergo a physical or chemical change upon interaction with electrons are used. The technique create patterns to the e-beam resists using focused electron beam. No mask plate is required; but, the desired patterns have to be transferred as a software code to

the EBL control unit. Except the stage translation unit and the pattern generator, all other components are the same with SEM systems. Thus, some SEM systems are upgraded with this lithography tool [50, 51].

2.3.3 Etching

Etching is used for mesa isolation and passivation opening. Mesa isolation step is crucial because the devices should be electrically isolated from each other. To isolate the devices, the top layers should be etched down to the semi-insulating (or highly resistive) buffer layer. Since the bond energies in III-nitrides are very strong, wet etching results in small etching rates, rough surface and side walls, inhomogeneous depth and negative slope [52, 53]. Thus, dry etching is preferred. Reactive ion etching (RIE) and inductively coupled plasma (ICP) etching technique have been extensively used for etching III-nitrides. The basic principle behind these techniques are as follows. First, a sample is placed inside the chamber and several gases are introduced. Gas molecules are broke into their ions using RF power resulting in plasma generation. The ions are accelerated through the sample and interact with its surface. This is chemical etching of reactive ion etching process. Besides, physical etching occurs when highly energetic ions hit the surface, they knock atoms out of the surface. Chlorine or fluorine based etchants serve for different needs. RF power, DC bias, gas mixtures, flow rate and temperature are the control parameters of the process [54, 55]. The system configuration is shown in Figure 2.13.

2.3.4 Metallization

Metal deposition onto semiconductors is necessary during fabrication for the formation of ohmic contacts, Schottky contacts, contact pads and interconnects. Various techniques are available for metallization including e-beam evaporation, thermal evaporation, sputtering and electroplating. E-beam evaporation is preferred for the metallization in this work. In e-beam evaporation, source material is bombarded with an e-beam given off a tungsten filament and deflected with the magnets in high vacuum. E-beam results in the local evaporation or sublimation

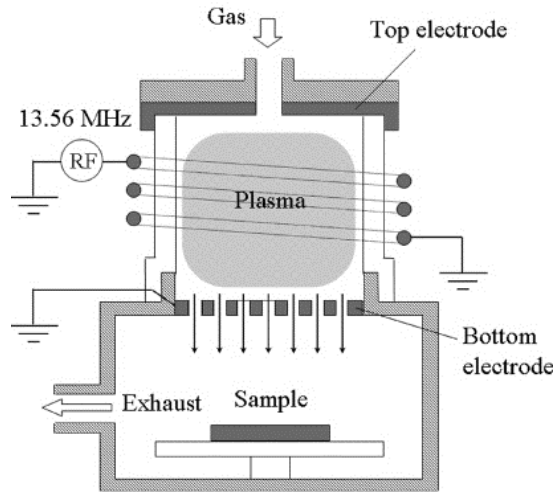


Figure 2.13: The configuration of inductively coupled plasma-reactive ion etching (ICP-RIE) system [56].

of the target surface. Depending on the temperature and vacuum level, target material then vaporize. Everything in the vacuum chamber are then coated with the thin solid film formed by the precipitation of evaporated atoms. High deposition rates are possible with this technique [57]. The schematic illustration of the system is provided in Figure 2.14.

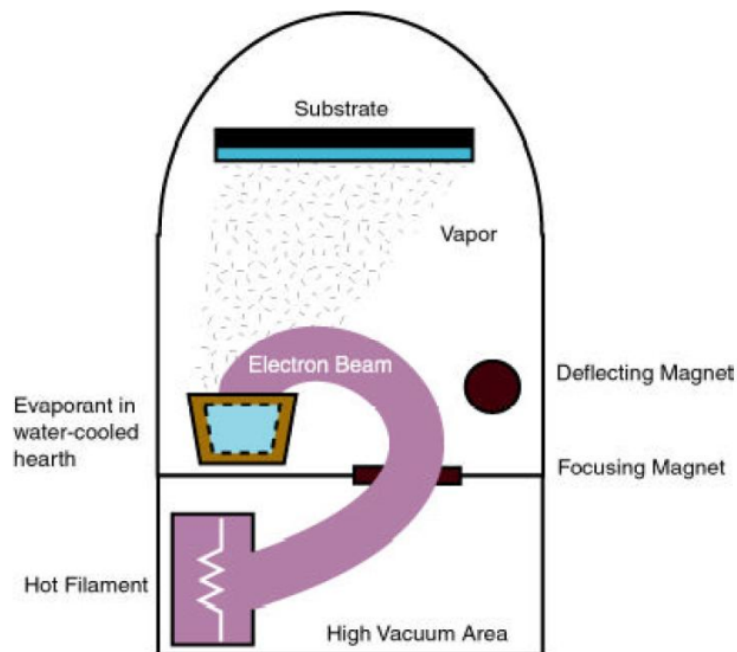
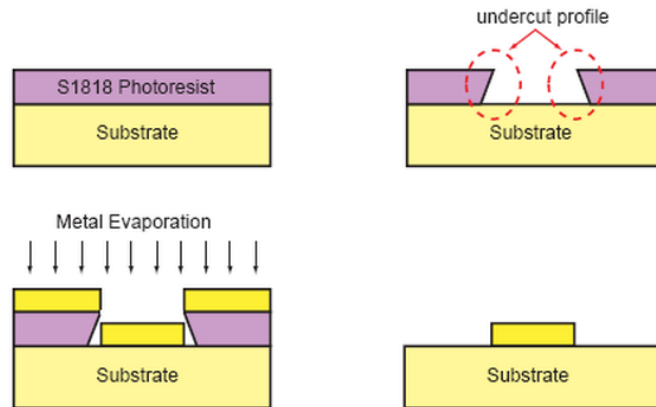


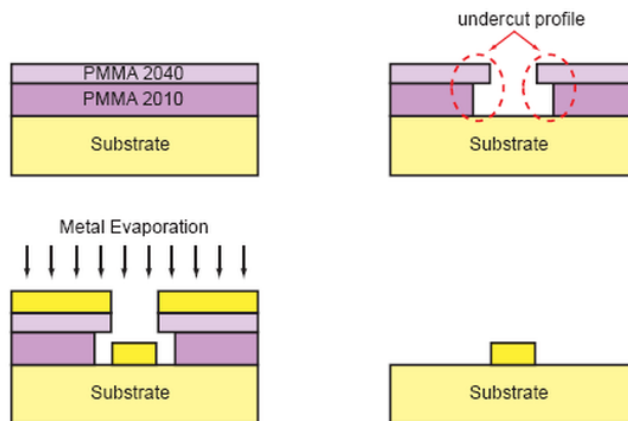
Figure 2.14: Configuration of the electron beam evaporator system.

The samples are masked with the resists patterned by either optical or e-beam lithography and then proper metal stack is evaporated. Following deposition, resists are removed with the lift-off procedure [58]. Lift-off procedure with different resists both used for optical and e-beam lithography method are schematically shown in Figure 2.15.

Formation of ohmic contacts necessitates rapid thermal annealing (RTA). RTA is a subset of the rapid thermal processing (RTP) system. The system includes a chamber and a powerful heating lamp. Rapid heating and slow cooling modify the electrical properties of the metal stack layers.



(a) Photoresist lift-off technique



(b) E-beam resist lift-off technique

Figure 2.15: Lift-off procedure for substrates masked with a) optical lithography and b) e-beam lithography.

2.3.5 Passivation

Passivation layer is an insulating layer coated on the active area of the devices. The passivation layer is needed to protect the device from surroundings. Various types of passivation layers can be used such as aluminium oxide (Al_2O_3), silicon nitride (Si_3N_4), scandium oxide (Sc_2O_3) and magnesium oxide (MgO) [39]. In particular, Si_3N_4 is used in this study as the passivation layer and deposited via plasma enhanced chemical vapour deposition (PECVD) method. Plasma is generated within PECVD system using electrical energy. Following plasma generation gas mixture is transferred into reactive radicals, ions, neutral atoms/molecules and other highly excited species. Interaction between the substrate surface and these reactive species results in either etching of the film or thin film formation. Thin films can be obtained at low temperatures. Generally mixtures of silane (SiH_4), ammonia (NH_3), nitrous oxide (N_2O) gases are used with different carrier gases such as N_2 , Ar, He [58]. The schematic illustration of the PECVD system is provided in Figure 2.16.

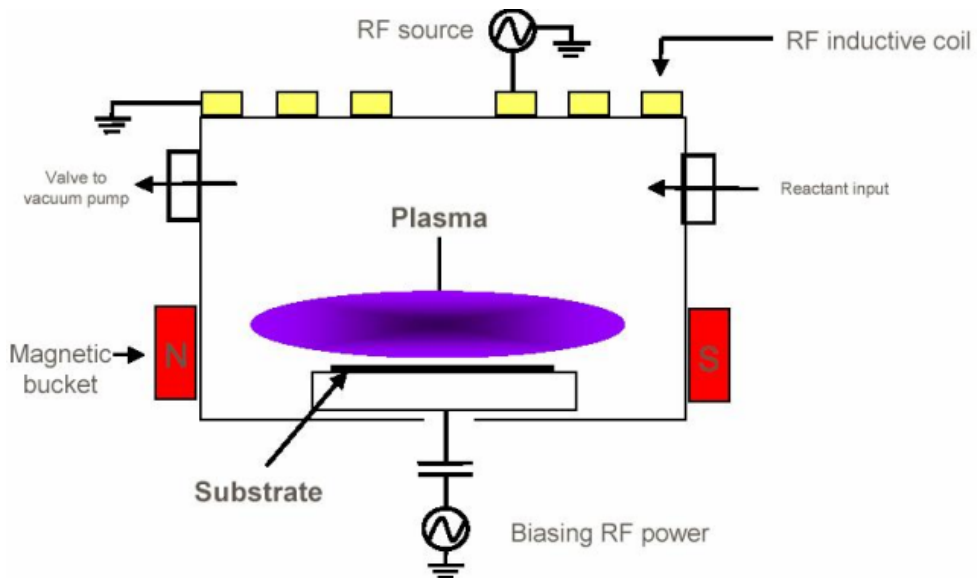


Figure 2.16: Schematic illustration of PECVD system [59].

2.4 Device Characterization

The characterization of the fabricated HEMT devices are explained in detail in this section. The characterization methods includes transmission line model (TLM), ellipsometry and DC measurements.

2.4.1 Transmission Line Model

Transmission line model is a widely used method to determine the quality of the ohmic contacts. This method includes measuring the resistance between rectangular metal contact pads deposited at different distances in between. Sheet resistance (R_s), contact resistance (R_c), specific contact resistance (ρ_c) values can be obtained from this method. The TLM patterns are illustrated in Figure 2.17. The rectangular contact pads with width W , length d and separated with increasing distance L_i , and the mesa width Z are shown in the Figure [60]. After measuring resistance, it is plotted against L and the data can be fitted linearly as described by the equation:

$$R = 2\frac{R_c}{W} + d\frac{R_{sheet}}{W} \quad (2.10)$$

Afterwards, the specific resistance can be calculated using

$$\rho_c = \frac{R_c^2}{R_{sheet}} \quad (2.11)$$

The specific contact resistivity determines the electrical quality of the metal contact. Specific contact resistivity of $2.96 \times 10^{-7} \Omega \text{ cm}^2$ and contact resistance of $0.22 \times 10^{-7} \Omega \text{ mm}$ were reported as excellent values [61].

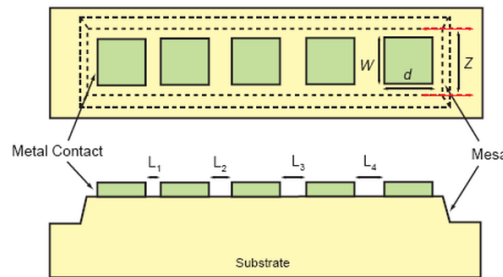


Figure 2.17: Top and cross-section view of TLM patterns.

2.4.2 Ellipsometry

Ellipsometry is used to get information about non-conducting thin films. It is primarily used to obtain optical constants and thickness of the thin films. The basic principle is analysing the change in the polarization of the incident and reflected or transmitted light. The change in polarization is quantified by an amplitude Ψ and a phase difference Δ [62]. The system consist of a light source, an interferometer, a polariser, an analyser and a detector. Characterization of the passivation layer in terms of its refractive index and thickness is conducted through ellipsometry in this thesis.

2.4.3 Direct Current Measurement

Direct Current (DC) measurements are conducted to assess electrical properties of the fabricated devices. The measurement setup is composed of a semiconductor parameter analyser and a probe station. Schematic of the setup used in this work is provided in Figure 2.18. Probe station allowed easy addressing of small contacts.

For I-V measurements, under an applied gate biases, drain voltage is swept

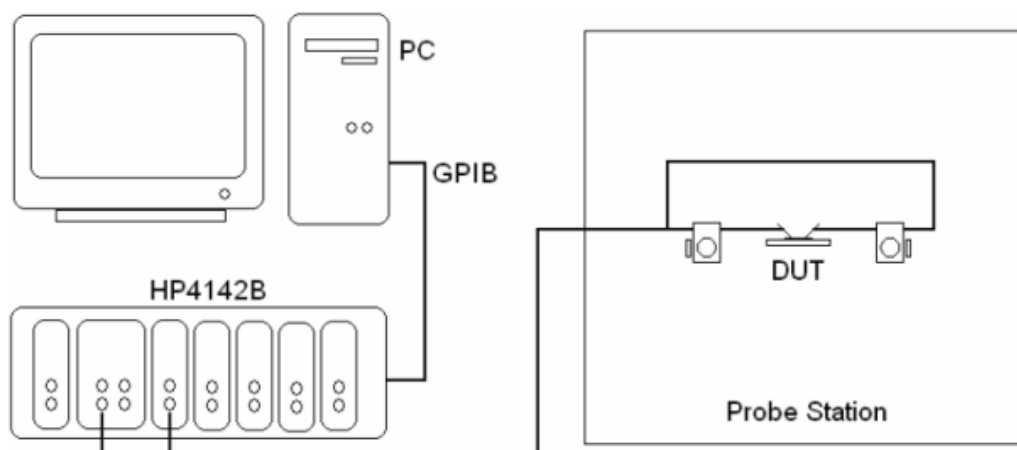


Figure 2.18: Schematic description of the DC characterization setup.

and drain current is measured. This measurement is repeated at different gate bias. Important parameters to be measured are knee voltage (V_{knee}), pinch-off voltage ($V_{pinchoff}$), maximum drain current (I_{ds}), transconductance (g_m) and breakdown voltage (V_{br}). A typical output IV curve of HEMT device is shown in Figure 2.19. The knee voltage signifies the voltage where saturation occurs in the graph. Also, maximum drain current is the intersection of the linear and saturation regions. Pinch-off voltage is where the drain current is almost zero. Transconductance is the ratio of the current change and is defined as

$$g_{m,DC} = \left. \frac{\Delta I_{DS}}{\Delta V_{DS}} \right|_{V_{DC}=constant} \quad (2.12)$$

Moreover, breakdown voltage is the maximum voltage that a device can handle when gate bias voltage is below pinch-off and drain voltage is increased until drain current reaches its maximum value I_{ds} .

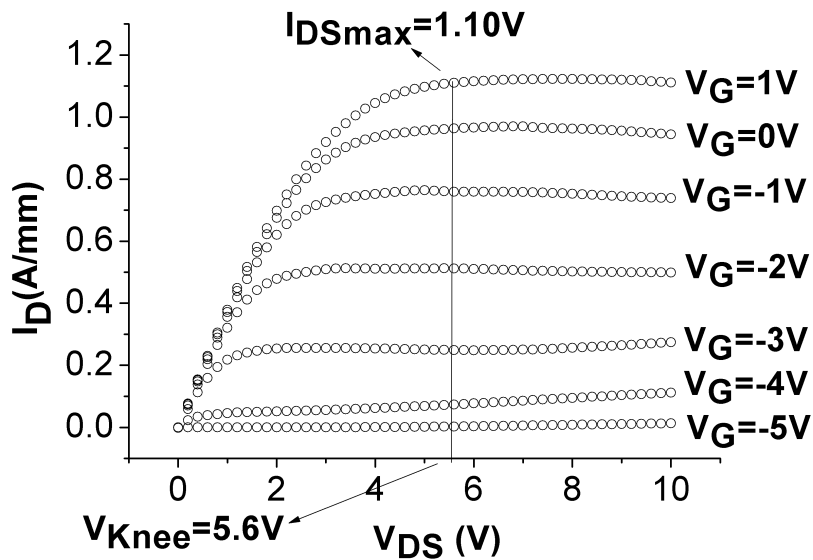


Figure 2.19: A typical output characteristic of HEMT devices.

CHAPTER 3

EXPERIMENTAL DETAILS

In this chapter, growth of AlGa_N/Ga_N HEMT structures and fabrication of AlGa_N/Ga_N HEMT devices on SiC substrates will be presented in detail. In the first section, epitaxial growth of AlGa_N/Ga_N HEMT structures will be discussed. Then, device processing using appropriate epitaxial structures will be elaborated.

3.1 Epitaxial Growth of AlGa_N/Ga_N HEMT Structures on SiC Substrates

The growth of HEMT structures are realized onto 6H-SiC substrates. The growth process is divided into two parts. In the first part, three different highly resistive Ga_N layers are grown. In the second part, two different HEMT structures are grown on optimized highly resistive Ga_N buffer layers.

3.1.1 Growth of Highly Resistive Ga_N Layer

To obtain a good pinch-off channel, a highly resistive Ga_N buffer is necessary. After surface treatment, AlN nucleation layers are deposited. This layers are followed by Ga_N buffer layers. Cross sectional schematic of highly resistive Ga_N buffer structure is provided in Figure 3.1.

Three different samples named as A, B, C are grown with different nucleation and annealing times to achieve Ga_N buffer with appropriate sheet resistivity,

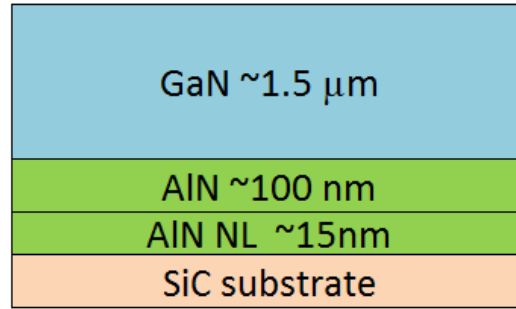


Figure 3.1: Cross sectional schematic of highly resistive GaN buffer structures

crystal quality and reasonable dislocation density. Epitaxial growths were performed using an AIXTRON RF200/4 RF-S horizontal reactor system and all growths were monitored with the Laytec in-situ reflectometry equipment with a 566 nm light source. Moreover, all the metallizations were employed using an OERLIKON LEYBOLD UNIVEX 350 e-beam evaporation system.

All growth procedures are initiated with the sample preparation. The standard cleaning procedure was applied. 2 inch 6H-SiC substrates are ultrasonically cleaned with acetone and isopropanol for 2 minutes, then rinsed with DI water and dried with N_2 gas. All of the layer depositions were employed using TmGa, TmAl, TmIn and NH_3 as the precursors for Ga, Al, In and N, respectively, N_2 and H_2 as carrier gases.

Once substrates are loaded into the reactor, the growth starts with the pretreatment steps. Samples are first annealed for 15 min at 1100°C at a pressure of 100 mbar under H_2 flow. During this thermal annealing, the etching of the SiC surface occurs which remove the scratches from the surface and smooth out the surface. Scratches usually formed during SiC substrate production. Then, the reactor temperature was decreased to 750°C and a nitridation step was carried out for 20 s under NH_3 flow of 500 sccm. The aim of this nitridation is to have a smooth and contamination free surface.

Following the nitridation step, AlN layers were deposited. To eliminate lattice mismatch effects, as Amano and Akasaki proposed, two-step growth of AlN layer was employed [17]. In this particular case, the deposition of a low temperature

(LT) (up to 800°C for SiC substrates) AlN nucleation layer (NL) is followed by a high temperature (HT) (usually > 1000°C) AlN layer. First, the SiC is covered with randomly distributed AlN nuclei, during annealing these nuclei further develop to islands and finally, high temperature AlN growth results in the coalesce of the annealed layer. Thus, a smooth layer is deposited. The key parameters are nucleation layer thickness, temperature and annealing time. Low temperature AlN nucleation layer time and annealing time are interdependent, nucleation layer time and annealing time are simultaneously varied and optimized in this study [37].

Since low temperature thin AlN nucleation layer has a high level of screw/mixed and edge/mixed type threading dislocations, dislocation density is decreased during high temperature AlN growth. Normally unintentional doped GaN (uid) have high background carrier concentration level ($\sim 10^{17} \text{ cm}^{-3}$) due to the residual donors [32]. To achieve semi-insulating or highly resistive GaN, different approaches are used. Compensating the residual donors with intentional doping the material with iron (Fe) or carbon (Ca) creates deep point like defects and is widely used since the sheet resistance values on the order of $10^{10} \Omega/\square$ can be obtained. However, this results in a strong memory effect in the reactor due to the contamination [33]. The safer method is optimizing the nucleation layer growth parameters to introduce dislocations (edge, screw or mix) or carbon impurities without deteriorating the crystal quality [34]. Since AlN is a wide bandgap material (6.2eV), it also promotes high resistivity [63, 64, 65].

Three samples are grown while the temperature, V/III ratio and pressure is kept constant. During the HT AlN growth, TmIn was introduced to the reactor. Due to the high kinetic energy of In atoms at high temperatures, the mobility of Al atoms increases. Moreover, at these temperatures, In atoms do not penetrate into the structure since In atoms have high evaporation rates. This AlN layers act as a template between SiC substrate and epitaxial layer and reduce the background doping concentration of GaN buffer layer [32].

Reactor parameters are changed to GaN buffer layers and $\sim 1.5\mu\text{m}$ thick GaN layer were grown onto AlN layers. GaN growth parameters are the same for

all of the samples (A, B and C). Three subsequent GaN layers were grown as a buffer with increasing growth rates, temperature, TmGa and NH₃ flows, whereas pressure is kept constant. The growth parameters of GaN on AlN are listed in Table 3.1. Titanium/aluminium/nickel/gold (Ti/Al/Ni/Au) (12/120/35/65 nm) ohmic contacts are deposited to investigate resistivity of the samples. Metal stack is evaporated with e-beam evaporation system. A Van Der Pauw geometry mask is used for metallization and contacts are annealed at 850°C for 30 sec using SSI SOLARIS RTP system under forming gas (95% N₂+5% H₂). The Hall effect measurements are conducted at RT using ECOPIA HMS 3000 Hall Effect measurement system under 10 nA input current and 0.57 T magnetic field.

3.1.2 Growth of Full HEMT Structure

On the optimized GaN buffer layer, 3 standard HEMT structures are grown, samples are named as H1, H2 and H3. First, very thin AlN interlayer is grown between GaN buffer and AlGaIn barrier. Since this interlayer decrease alloy scattering, it improves mobility. Furthermore, AlN interlayer creates a strong polarization field and improve the sheet carrier charge density and hence the device performance as mentioned in Chapter 2 [28, 26]. Subsequent to interlayer, an AlGaIn barrier layer with different Al concentration and finally GaN cap layer is grown. Cross sectional schematic of full HEMT structure is provided in Figure 3.2.

Prior to the growth of full HEMT structures, a control sample with thicker layers

Table 3.1: The growth parameters of GaN on AlN layers.

Growth Parameters	Time	P (mbar)	T (°C)	TmAl (sccm)	NH ₃ (sccm)	TmIn (sccm)	TmGa (sccm)
GaN (3)	15 min	200	1075	-	2000	-	17
GaN (2)	20 min	200	1050	-	1250	-	17
GaN (1)	15 min	200	1020	-	1000	-	12
AlN (HT)	20 min	25	1130	20	600	50	-
Annealing	60-90 sec	25	1130	-	600	-	-
AlN NL	75-90 sec	50	740	15	500	-	-

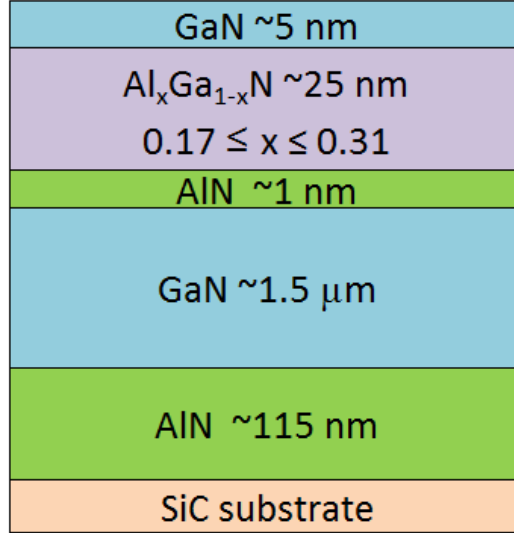


Figure 3.2: Cross sectional schematic of full HEMT structures.

are grown with same growth parameters to obtain the growth rates of the AlN, AlGa_xN and GaN layers. Accordingly afterwards, the thickness of the actual HEMT layers are determined. Growth parameters are listed in Table 3.2.

2 inch wafers were cut in to 12x12 mm pieces and Ti/Al/Ni/Au (12/120/35/65 nm) metal stack is deposited with Van Der Pauw geometry using e-beam evaporation. Right after, rapid thermal annealing of the wafers at 850°C for 30s under forming gas is conducted for the formation of ohmic contacts to investigation of electrical properties of 2DEG. Hall Effect measurements are applied under 1mA input current and 0.57 T magnetic field at room temperature. Upon the measurement results, the two structures with better electrical properties are fabricated.

Table 3.2: The growth parameters of the layers deposited onto highly resistive GaN buffer

Growth Parameters	Time (sec)	P (mbar)	T (°C)	TmAl (sccm)	NH ₃ (sccm)	TMGa (sccm)
GaN cap layer	15	50	1090-1105	10-12	500	4-5
AlGa _x N barrier layer	120	50	1090-1105	10-12	500	4-5
AlN interlayer	14	50	1090-1105	10-12	300	-

3.2 Fabrication of HEMT devices

The processing of HEMT devices from HEMT structures is described in this chapter. The fabrication steps are applied as described in the previous chapter. The schematic illustration of fabrication steps are provided in Figure 3.3.

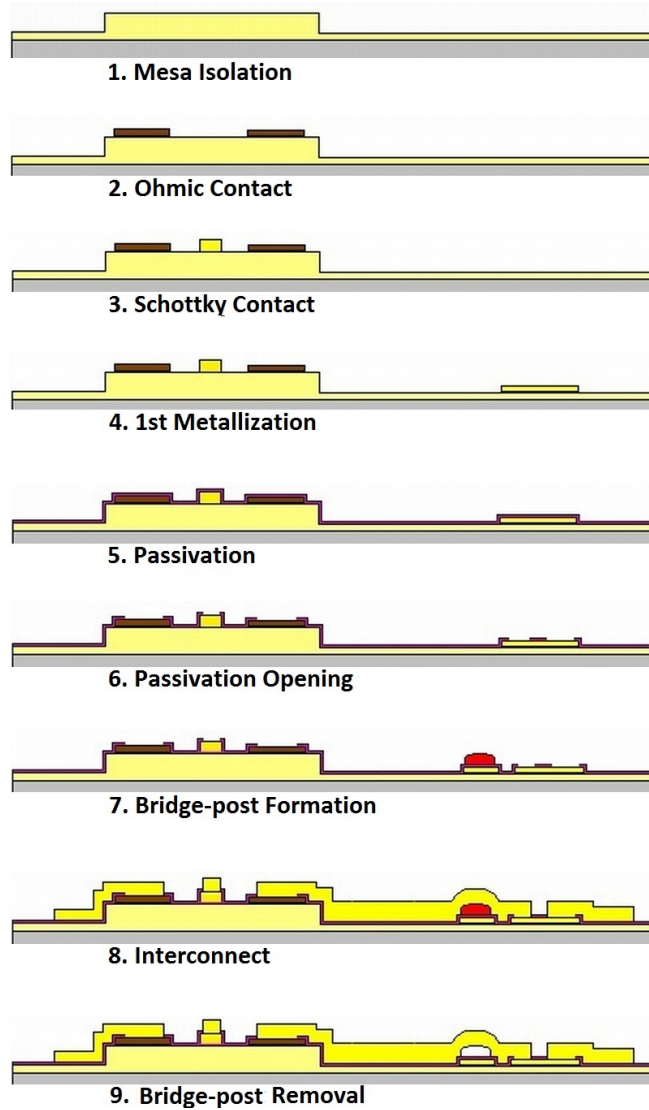


Figure 3.3: Schematic illustration of fabrication steps.

3.2.1 Sample Preparation

Fabrication starts with the standard cleaning procedure as described previously.

3.2.2 Mesa Isolation

Next step during fabrication is the mesa isolation. Isolation of the mesa islands is achieved by SENTECH Plasma SI 500 ICP RIE system. Optical lithography is used for patterning using AZ5214 photoresist. AZ5214 is a special kind of photoresist which can be used both in negative and positive tone. For mesa isolation, AZ5214 is applied in positive tone. Plasma is obtained using a gas mixture BCl_3 (20 sccm)/ Cl_2 (25 sccm)/Ar (10 sccm) at a pressure 0.40 Pa, under a 100W RF power. Using these conditions, an etch rate of around 100 nm/min is obtained. A 50 s etching resulted in an average etch depth of 90 nm which is appropriate for mesa island isolation since the 2DEG position is nearly 30 nm below the surface. After etching process, standard cleaning process was applied again which is followed by O_2 plasma cleaning to remove residual photoresist on the wafer surface. Optical microscope image of mesa islands is provided in Figure 3.4.

3.2.3 Ohmic Contact Formation

Following mesa isolation, source and drain ohmic contacts are placed on the top of the mesa structures and patterned by optical lithography. AZ5214 photoresist is used in negative tone to obtain negative profile, since the lift-off technique is used after metallization. Ti/Al combination is widely used for the ohmic con-

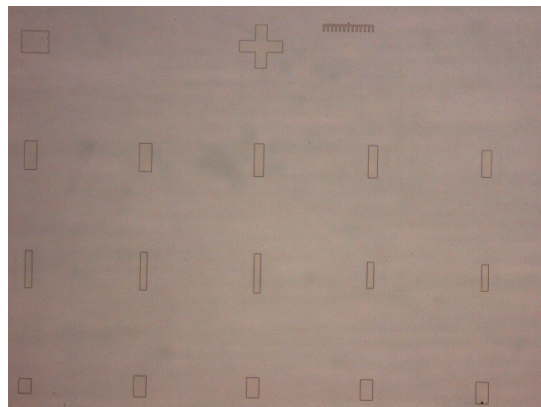


Figure 3.4: Optical microscope image of mesa structures of the the fabricated HEMT devices.

tacts. Ti forms TiN if it is deposited onto GaN or AlGaIn and annealed at proper temperatures. Formed TiN islands induce *n*-type doping at the Ti/GaN interface due to N-deficiency. This affects the tunneling mechanism and results in an ohmic behaviour. Al provides higher conductivity and protects Ti surface from oxidation. On top of that Ni/Au is evaporated. This layer prevents the oxidation of Al layer while annealing. Ni acts as a barrier between Al and Au layers that restrains the outdiffusion of Ti, Al and indiffusion of Au. Besides oxidation protection, topmost Au layer improves the conductivity [66, 67, 68]. Ti/Al/Ni/Au (12/120/35/65 nm) metal stack is evaporated with e-beam evaporation system. Drain to source separation is 3 μm for all devices. This multilayered metal contacts are annealed at 850°C for 30 s under forming gas. Optical microscope images of ohmic contacts before and after annealing is provided in Figure 3.5(a) and 3.5(b), respectively.

3.2.4 Schottky Contact Formation

Following ohmic contacts, gate formation step is initiated. Gate lengths are chosen to be 300 nm. Gate patterns are applied using e-beam lithography with PMMA resist. To increase the Schottky barrier height, Ni which have high work function is used. Topmost Au layer is deposited to improve the conductivity and to prevent Ni from oxidation. Ni/Au (50/300 nm) metals are evaporated using e-beam evaporation system. Optical microscope image and SEM images

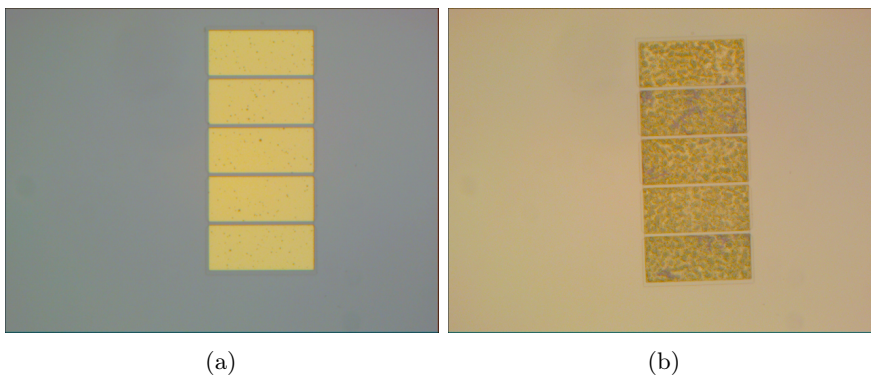


Figure 3.5: Optical microscope images of ohmic contacts (a) before and (b) after annealing.

of gates are provided in Figure 3.6(a) and 3.6(b), 3.6(c), respectively.

3.2.5 1st Level Metallization

The next step is 1st level metallization, to create gate bus metals at the end of gate fingers. Patterns are created with optical lithography using photoresist AZ5214 in negative tone to obtain a negative profile. Ti/Au (50nm/350 nm) metal layers are evaporated with e-beam evaporation system. Optical microscope image is provided in Figure 3.7. Following metallization, lift-off procedure of gate electrodes is applied for the resist removal.

3.2.6 Passivation

Subsequently, to increase the performance of the devices a 300 nm thick Si_3N_4 thin film as the passivation layer was deposited using SENTECH SI 500 PPD

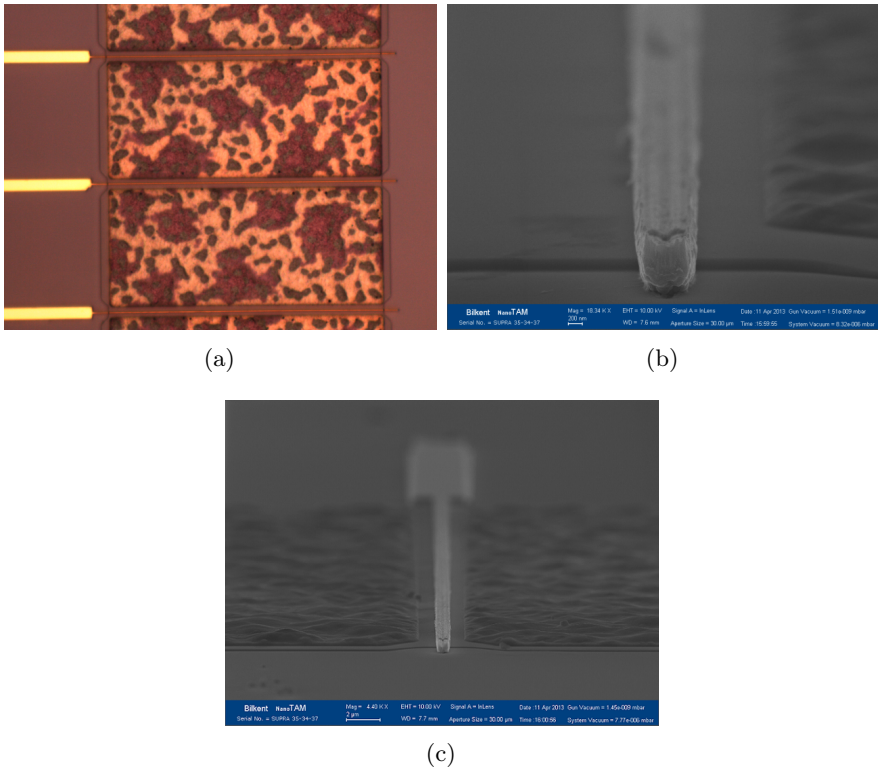


Figure 3.6: (a) Optical microscope and (b), (c) SEM images of gate electrodes.

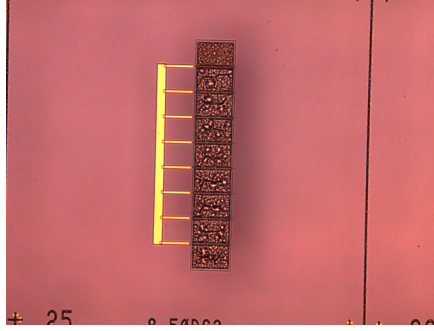


Figure 3.7: Optical microscope image of 1st level metallization.

PECVD system. Deposition temperature and pressure are 300°C and 80 Pa, respectively. A $\text{SiH}_4(300\text{sccm})/\text{NH}_3(15\text{ sccm})/\text{Ar}(50\text{sccm})$ gas mixture is used to generate plasma under an RF power of 500W. Optical microscope image of passivated sample is provided in Figure 3.8.

3.2.7 Contact Pad Opening

After the passivation step, the samples are subjected to an etching procedure to etch away the contact pad regions using ICP-RIE system. Patterning of the openings are applied by optical lithography. Patterns are created using AZ5214 in positive tone. Plasma is generated using CHF_3 gas at a pressure of 0.40 Pa under 100W of RF power. Average etch depth is measured to be 310 nm on the contact pad areas. An optical microscope image of the sample after opening the contact pads is provided in Figure 3.9.

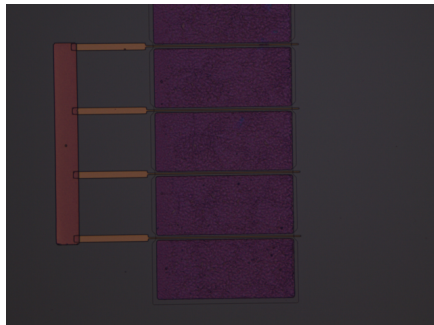


Figure 3.8: Optical microscope image of the sample following Si_3N_4 passivation.

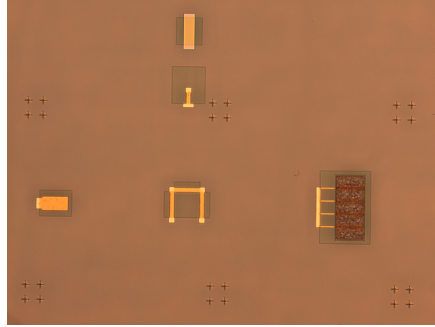


Figure 3.9: Optical microscope image of the sample after Si_3N_4 passivation opening step.

3.2.8 Air-Bridge Formation

After contact pad opening, air bridge post formation step is carried out. Air bridges are used to connect isolated contact pads to each other. At first, optical lithography is conducted with a special photoresist, S1828. After developing the samples in AZ326MIF developer, samples are baked at 200°C for 5 minutes. This baking step changes the profile of the resist and the corners become round (reflow process) preventing the disconnection of the metalization during lift-off. Optical microscope images of the bridge posts are provided in Figure 3.10.

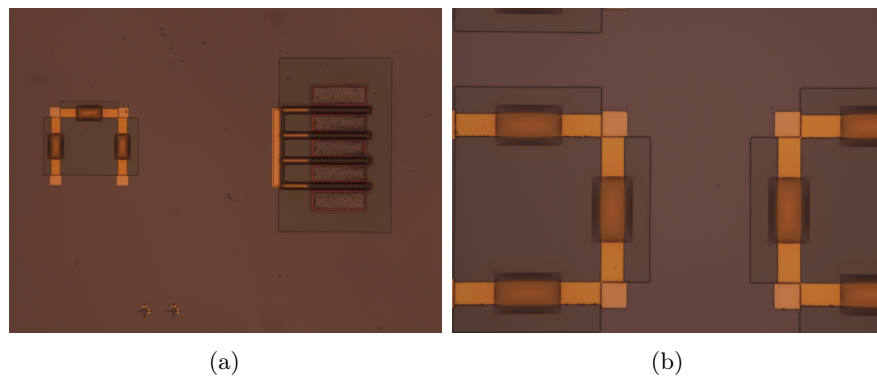


Figure 3.10: Optical microscope images of (a) bridge posts and (b) close-view of bridge posts.

3.2.9 Interconnect Metallization

The final step of the fabrication process is interconnect metallization. For patterning, optical lithography is applied onto samples when bridge posts are still there. Special negative resist (AZ2070nlof) is used for this purpose. Then thick Ti/Au (200/2000 nm) metal stack is evaporated using e-beam evaporation system. After lift-off process in NMP (1-methyl-2-pyrrolidon) stripper, bridge posts are removed using AZ100 remover. An SEM image of the formed air bridges are provided in Figure 3.11. For finishing step, samples are carefully cleaned according to the standard cleaning procedure. An optical microscope image of the finalized devices is provided in Figure 3.12.

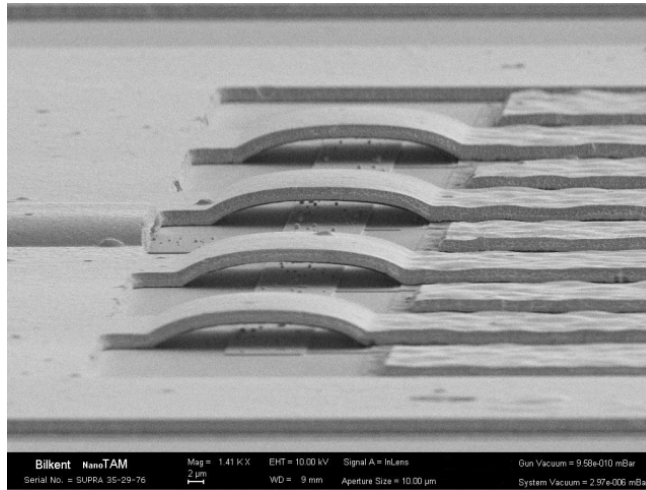


Figure 3.11: SEM images of air-bridges.

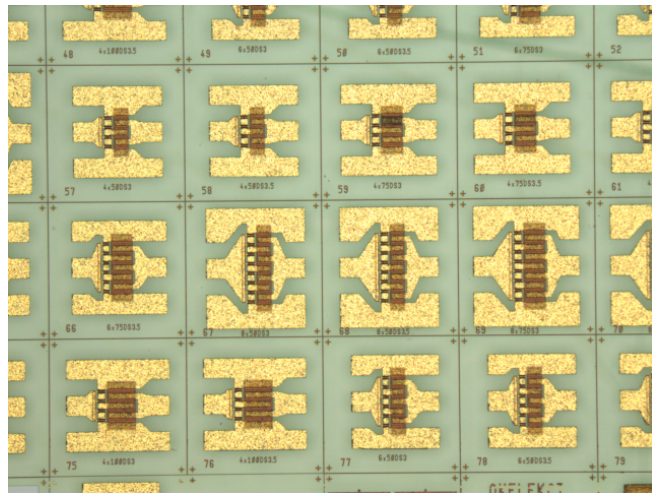


Figure 3.12: Optical microscope images of the finalized devices.

CHAPTER 4

RESULTS AND DISCUSSION

In this chapter, characterization results of AlGaN/GaN HEMT structures and HEMT devices will be presented. In the first section, characterization and optimization of highly resistive GaN structures will be explained. Then, using structural and electrical characterization methods, full HEMT structure properties will be discussed. Finally, electrical properties and performance of the fabricated devices will be analysed.

4.1 Characterization of Highly Resistive GaN structures on SiC

Both in-situ and ex-situ characterizations of highly resistive GaN samples are conducted. Then, optimized highly resistive GaN structures are used for the growth full HEMT structures.

The first characterization of the three highly resistive GaN samples (A, B and C) are accomplished by in-situ reflectometry measurements as mentioned in Chapter 2. Using optical reflectance curves the transition between AlN to GaN layers is monitored. The reflectance transients of sample B are shown in Figure 4.1.

After desorption step, a very small increase is observed in reflectance transients. This increase is due to the difference between refractive index of SiC substrate and AlN layers. AlN nuclei covers the SiC surface (wetting) at this step. The increase of the signal intensity depends on the thickness of the nuclei, in other words, the time of AlN nucleation layer growth. Following annealing step, AlN nuclei develop islands. At the end of the annealing, high temperature AlN layer

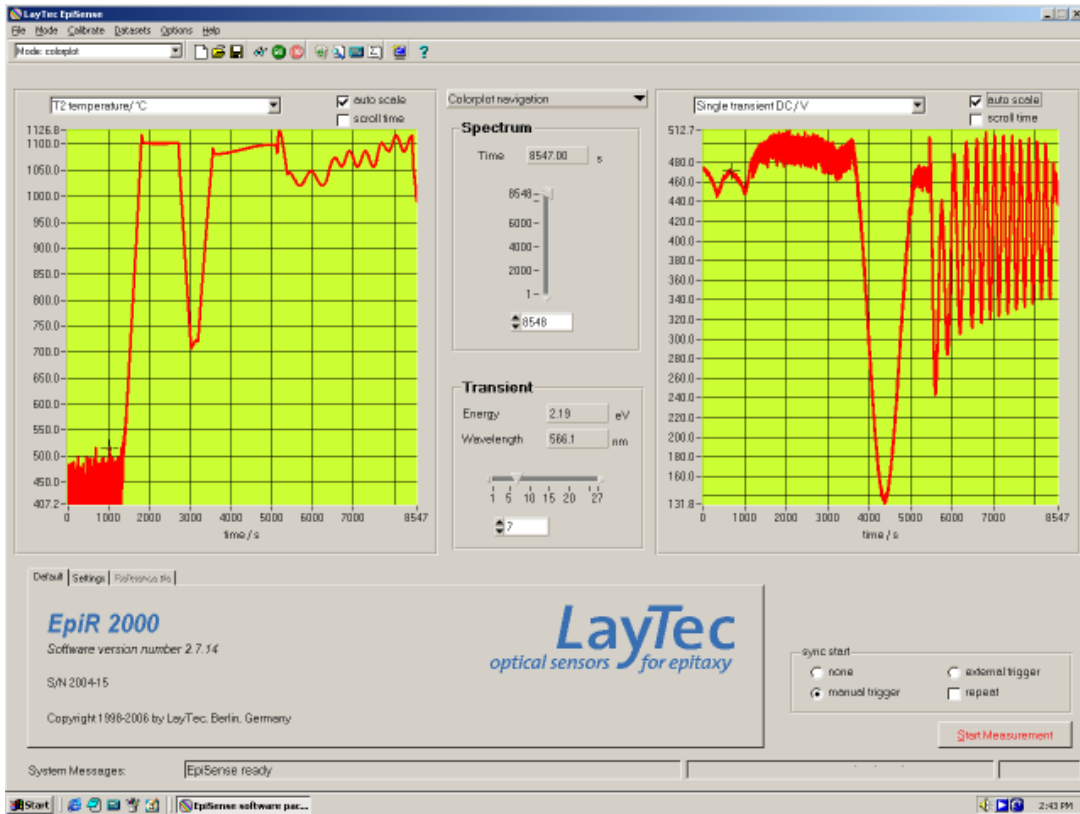


Figure 4.1: Reflectance transients for highly resistive GaN layers on SiC substrate.

starts to grow, the intensity drops while the temperature is ramped. This drop can be explained with two mechanisms which are the coalesce of the islands to form larger structures and evaporation of the material at this high temperature. The thickness of the AlN nucleation layer decreases with the modified rough surface where the intensity drops to almost the intensity value coming from the reflectance signal directly from the SiC substrate. Depending on the time of high temperature AlN layer, as more islands coalesced, the surface becomes smoother and simultaneously thickness increases, thus the intensity starts to increase again. When GaN growth starts, three dimensional growth mode takes place with the formation of GaN islands. Hence, the surface roughness increases which results in a decrease in reflectance signal. These GaN islands further coalescence as the thickness increases and transition to two dimensional growth mode occurs with the recovering of the intensity signal. The periodic oscillations from the reflected light is initiated, as growth continues, the maximum amplitude of the oscillations obtained when the uniform layer of two dimensional GaN layer

is deposited. The maximum and minimum value of the signals remain at the same position and amplitude of intensity modulation does not change indicating a high surface quality of GaN layers [37]. Moreover, the average growth rates are calculated from oscillations for AlN layers as $0.31 \mu\text{m}/\text{h}$. Furthermore, growth rates for GaN layers are found to be 1.50, 1.85, and $2.07 \mu\text{m}/\text{h}$, respectively. The thickness of the layers are calculated as $\sim 108 \text{ nm}$ for AlN and $\sim 1.5 \mu\text{m}$ for GaN layers.

For ex-situ characterization; cross-sectional SEM analysis for thickness calculation, HRXRD for the crystal quality determination, AFM for surface roughness and Hall Effect measurements for the determination of electrical properties are conducted.

A cross-sectional SEM image is provided in Figure 4.2. From cross-sectional SEM images, the thickness of the layers of the sample B are obtained as $\sim 119.6 \text{ nm}$ for AlN and $\sim 1.5 \mu\text{m}$ for GaN layers, which is consistent with the calculated values from growth rates.

AFM images of samples A, B and C from an area of $5 \times 5 \mu\text{m}^2$ are provided in Figure 4.3 (a) to (c), respectively. AFM images are obtained using contact mode of VEECO CPII AFM system.

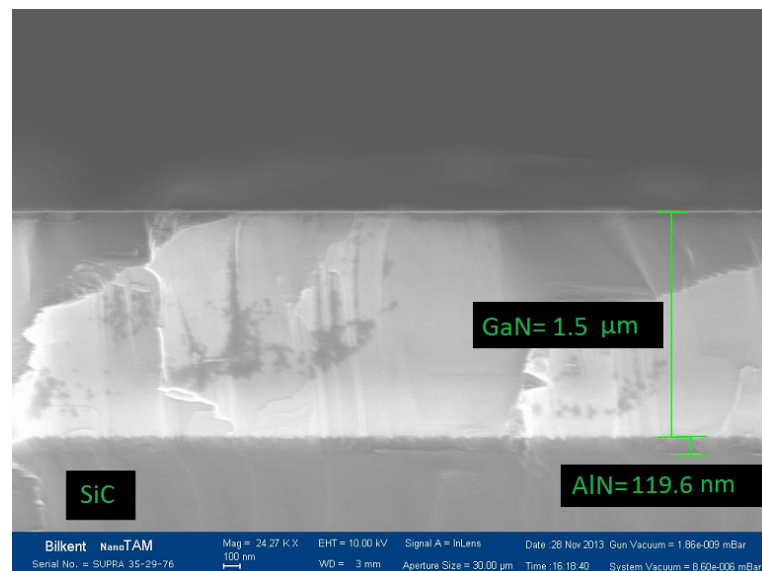


Figure 4.2: A cross-sectional SEM image of highly resistive GaN layers.

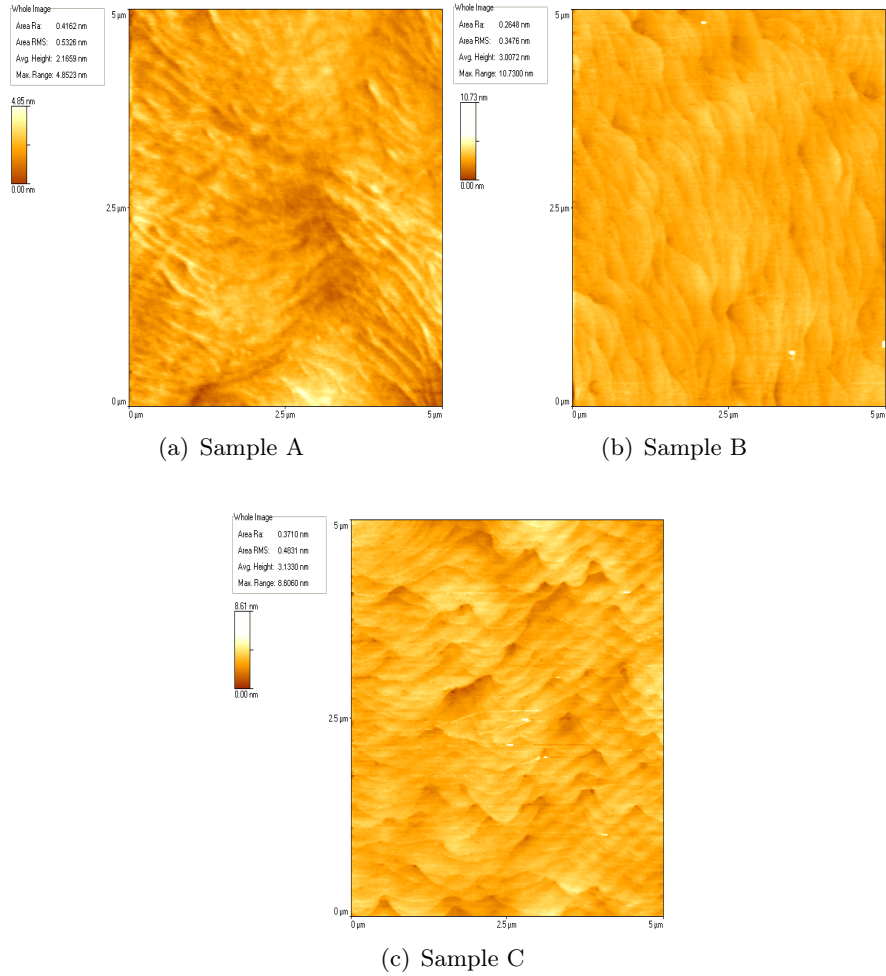


Figure 4.3: AFM images of samples (a) A, (b) B, and (c) C.

The rms roughness values are found as 0.53, 0.35 and 0.48 nm for samples A, B and C, respectively. As seen from the images, all the samples have well defined step-terrace structures. Step-flows confirm that the growth ends in a kinetically controlled two dimensional growth mode. The step termination is due to the end of both screw and mixed type of threading dislocations. The edge type dislocations are directly related with the low angle grain boundaries which is formed during coalesce of the nucleation layer. High density of islands results in higher density of edge dislocations. Sample B has the lowest step-termination density than sample C. Sample A has a rough surface; therefore, it is not possible to recognize clearly the step termination. Along with the rms roughness values, Sample B has the best surface quality. The difference

of the surface roughness values revealed that the low temperature nucleation layer thickness and annealing of the nucleation layer time affect the surface roughness of the GaN layers which is also affected by the changes in dislocation density [69, 34].

In addition, the structural quality of the samples is investigated from HRXRD measurements using RIGAKU SMARTLAB X-RAY DIFFRACTOMETER. Full width half maximum (FWHM) values are collected from the symmetric (002) and asymmetric (102) diffraction peak of rocking curves. The XRD $\omega/2\theta$ scan results of the three samples are provided in Figure 4.4. (JCPDS Card no: 25-1133 for AlN, 02-1078 for GaN, 29-1128 for 6H-SiC)

Heteroepitaxial growth of AlN and GaN results in high levels of film strain due to the lattice mismatch between the substrate and layer. Besides, formation of dislocations, unintentional incorporation of point defects and impurities obtained. Analysis of the diffraction peaks, gives information of defects in a sample. The peak analyses is usually conducted via the FWHM values. FWHM value of the peaks are determined by several components which are; intrinsic rocking curve, instrumental broadening, mosaicity, strain broadening, crystal size broadening,

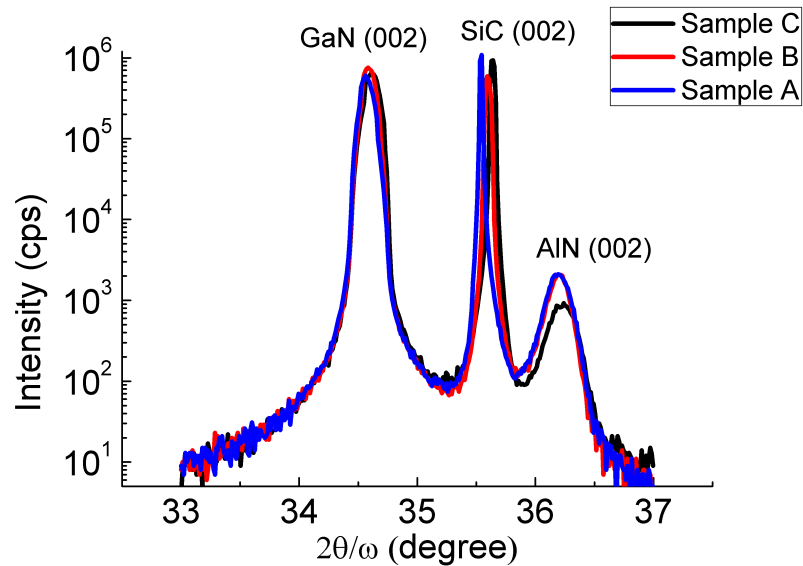


Figure 4.4: The XRD $\omega/2\theta$ scans of the HR GaN structures.

curvature of the crystal and dislocations in the crystals. Edge, screw and mixed type threading dislocations are present in the layers. Sharper peaks give smaller FWHM values and indicates good crystalline quality with low defects.

Specific crystallographic planes are distorted by a specific threading dislocations geometry. Edge dislocations have a plane strain; therefore symmetric (002) rocking curves are insensitive to the pure edge dislocations. Since these planes are undistorted by the edge dislocations, asymmetric (102) planes are distorted by the edge dislocations. Thus, asymmetric planes are sensitive to this type of dislocations. Whereas, screw dislocations have a pure shear strain such that, they distort all symmetric planes. As a result, symmetric rocking curves are sensitive only to screw dislocations [70]. Asymmetric (102) plane scans give information about edge and screw dislocations. On the other hand, symmetric scans (002) give information about screw dislocations [71, 72].

The XRD measurement results revealed that all three samples have good crystalline quality. Comparing samples A and B, it is found that nucleation layer thickness increased the FWHM value of ω scans of GaN (002) and AlN (002), whereas that of AlN (102) decreased and GaN (102) almost remained the same. These values indicated that, increasing nucleation layer thickness results in an increase in screw dislocation density; but, decrease in an edge dislocation density. Therefore, decrease in sheet resistance value is expected.

Furthermore, comparing sample B and C, where the difference is the annealing time of the nucleation layer, decreasing annealing time resulted in broadening of the both symmetric and asymmetric reflectance peaks from ω scans belongs to GaN and AlN. Thus, the crystal quality deteriorated.

For determination of the sheet resistance; Hall Effect measurements are conducted. The resistivity determines if the GaN layers are appropriate for acting as a buffer for HEMT structures. Highly resistive (10^8 - 10^{11} Ω/\square) GaN layers are required as stated in Chapter 2. The resistivity values are obtained as 1.01×10^{10} , 1.10×10^{11} and 3.06×10^9 for samples A, B and C, respectively. Hall effect measurements revealed that all the samples have high resistivity; but the highest value belongs to sample B. The reason for this can be explained through the

presence of which edge dislocations, work as acceptor like trap levels promoting higher resistivity [73]. The AFM, HRXRD measurement results and resistivity values of GaN samples are tabulated and provided in Table 4.1.

Table 4.1: The AFM and HRXRD characterization results of highly resistive samples.

Sample	Growth Parameters (sec)	AFM RMS Roughness (nm)	XRD FWHM of ω Scans (arcsec)	Sheet Resistance (Ω/\square)
Sample A	Anneal time:90 Nucleation time:90	0.53	GaN (002):299 GaN (102):490 AlN (002):947 AlN (102):1930	1.01×10^{10}
Sample B	Anneal time:90 Nucleation time:75	0.35	GaN (002):280 GaN (102):492 AlN (002):536 AlN (102):2700	1.10×10^{11}
Sample C	Anneal time:60 Nucleation time:75	0.48	GaN (002):378 GaN (102):619 AlN (002):2390 AlN (102):2812	3.06×10^9

From the characterization results, an optimal growth condition for AlN nucleation layer is found to be 75 s for LT AlN nucleation time and 90 s for the annealing time. These belong to sample B. Since both HRXRD FWHM values and AFM surface roughness values are in good agreement, full HEMT structures are grown using that GaN buffer template.

4.2 Characterization of AlGaIn/GaN HEMT structures on GaN buffer

Three HEMT structures named as H1, H2, H3 are grown on the optimized GaN buffer template. Growth rates are calculated from Fabry-Perot oscillations of in-situ reflectometry of control sample. The reflectance transients of HEMT control sample can be seen in Figure 4.5. From these transients growth rates are calculated to be $0.27 \mu\text{m/h}$ for AlN interlayer, $0.97 \mu\text{m/h}$ for AlGaIn barrier and $1.39 \mu\text{m/h}$ for GaN cap layer.

Using these growth rates, for all of the three samples, ~ 1 nm AlN, ~ 25 nm

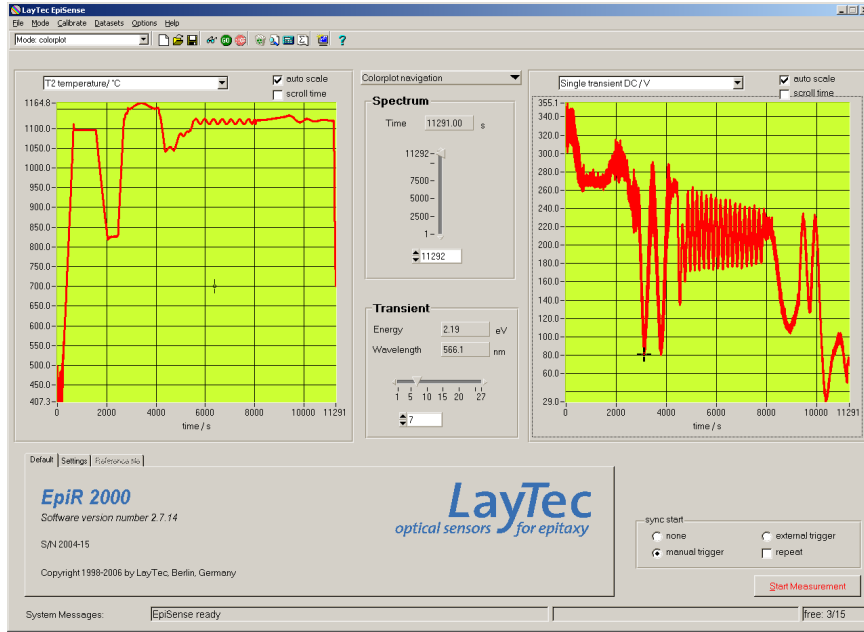


Figure 4.5: Reflectance transients of HEMT control sample.

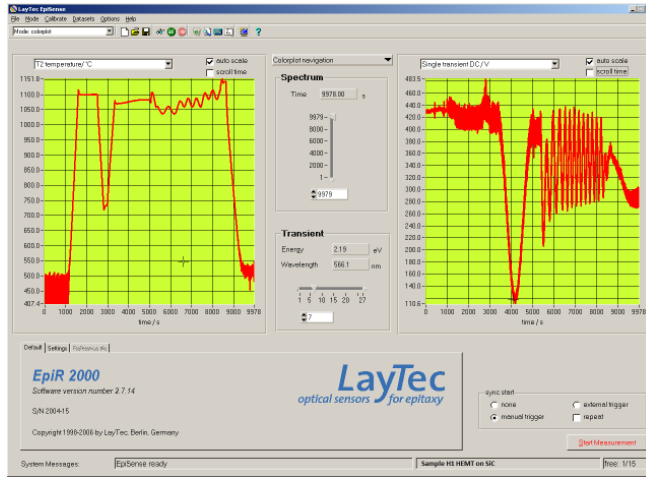
$\text{Al}_x\text{Ga}_{1-x}\text{N}$ and ~ 5 nm GaN cap layer are grown with adjusting the growth time accordingly. The reflectance transients of sample H1, H2 and H3 are provided in Figure 4.6 (a) to (c), respectively. The reflectance transients indicated that all samples ended in two dimensional growth mode and had good surface quality.

$\omega/2\theta$ scans for the samples are provided in Figure 4.7. The symmetric (002) and asymmetric (102) high resolution diffraction peak of rocking curves are used to obtain FWHM values of ω scans for (Provided in Table 4.2).

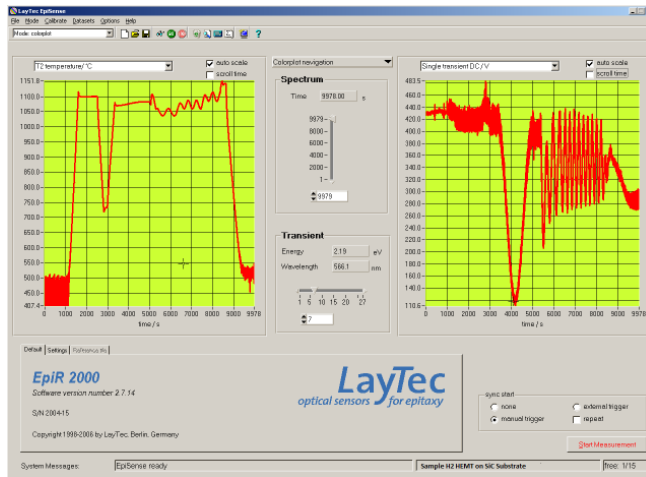
These values indicate that all samples have good crystal quality. Al concentration in $\text{Al}_x\text{Ga}_{1-x}\text{N}$ layers are calculated from Vegard's law using ω scans based

Table 4.2: The HRXRD ω scans of HEMT structures.

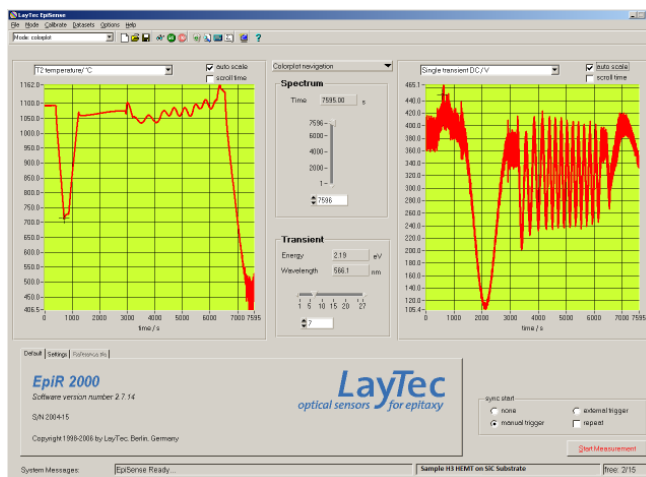
HRXRD FWHM (arcsec)					
	GaN (002)	GaN (102)	AlN (002)	AlN (102)	$\text{Al}_x\text{Ga}_{1-x}\text{N}$ (002)
Sample H1	252	349	356	1908	374
Sample H2	223	313	310	2880	345
Sample H3	191	284	425	2196	302



(a) Sample H1



(b) Sample H2



(c) Sample H3

Figure 4.6: Reflectance transients of samples H1, H2 and H3.

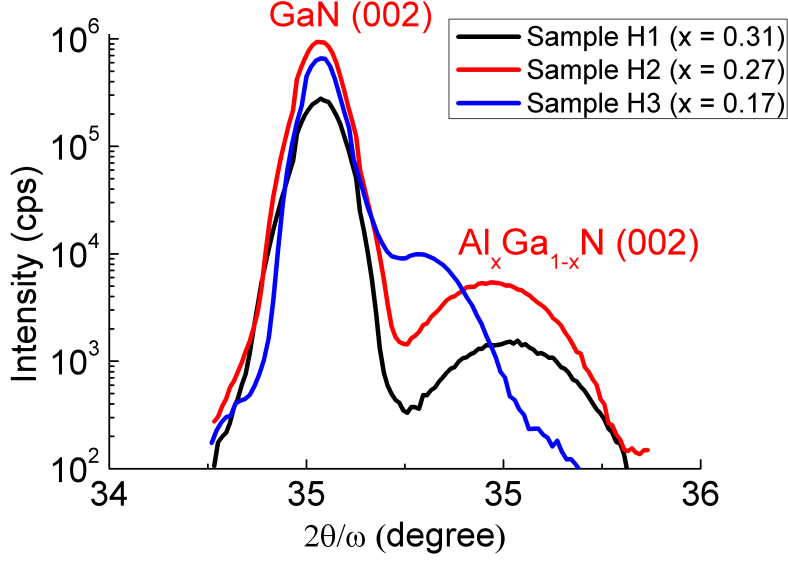


Figure 4.7: HRXRD Rocking Curves for HEMT structures.

on the peak position shift of the AlGaIn layer from the reference peak positions of GaN and AlN. The Al fraction of $\text{Al}_x\text{Ga}_{(1-x)}\text{N}$ is given by:

$$X = \frac{\Delta\theta}{\Delta\theta_0} \quad (4.1)$$

,where $\Delta\theta_0$ is the the difference in angle θ between AlN and GaN, $\Delta\theta$ is the angle shift of $\text{Al}_x\text{Ga}_{(1-x)}\text{N}$ from GaN. For Sample H1, H2, and H3, Al mole fractions are evaluated to be 0.31, 0.27 and 0.17, respectively.

As the Al content increase, the FWHM of AlGaIn (002) peak is increased (Figure 4.8) due to the large lattice mismatch between GaN and AlGaIn. The increase in Al content results in an increase in the lattice stress between GaN and AlGaIn layer which results in widening of (002) reflectance peak of AlGaIn. Furthermore, the dislocation density is higher for the sample H2 than sample H1 as observed from the FWHM value of AlN (102) peak. All the FWHM values denoted that the crystal quality which is related with the defects of GaN buffer layers were very similar for three samples [74].

As mentioned before, electrical properties are the most important characteristics for optimum HEMT device performance. In order to characterize 2DEG sheet carrier concentration (n_s), mobility (μ) and sheet resistance (R_s) of the struc-

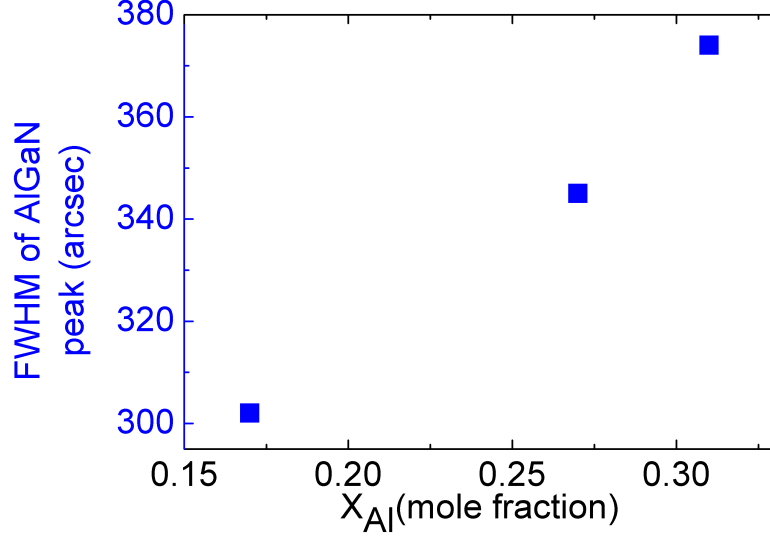


Figure 4.8: FWHM of AlGaIn(002) ω scan of HEMT samples as a function of Al content of AlGaIn.

tures, Hall Effect measurements are conducted on 12 x 12 mm sample pieces. Results are provided in Table 4.3.

Both n_s and μ increased with the increasing Al content as expected. This relation is presented by Figure 4.9. The reason for the increase in both sheet carrier density and mobility is the increase in spontaneous and piezoelectric polarization effects, which lead to better polarization induced electron confinement. Moreover, stress in the cap layer creates a piezoinduced charge which results in the increase of sheet carrier density. Various scattering mechanisms limits the 2DEG mobility. At room temperature, polar phonon scattering is responsible for limiting the mobility. At low sheet carrier densities, impurities together with the piezoacoustic scattering is the limiting mechanisms. However, at high sheet

Table 4.3: The Hall Effect results of HEMT samples.

Sample	X_{Al} %	n_s (cm^{-2})	μ (cm^2/Vs)	R_s (Ω/\square)
Sample H1	31	$1.39 \cdot 10^{13}$	1643	273
Sample H2	27	$1.26 \cdot 10^{13}$	1506	329
Sample H3	17	$1.17 \cdot 10^{13}$	1150	464

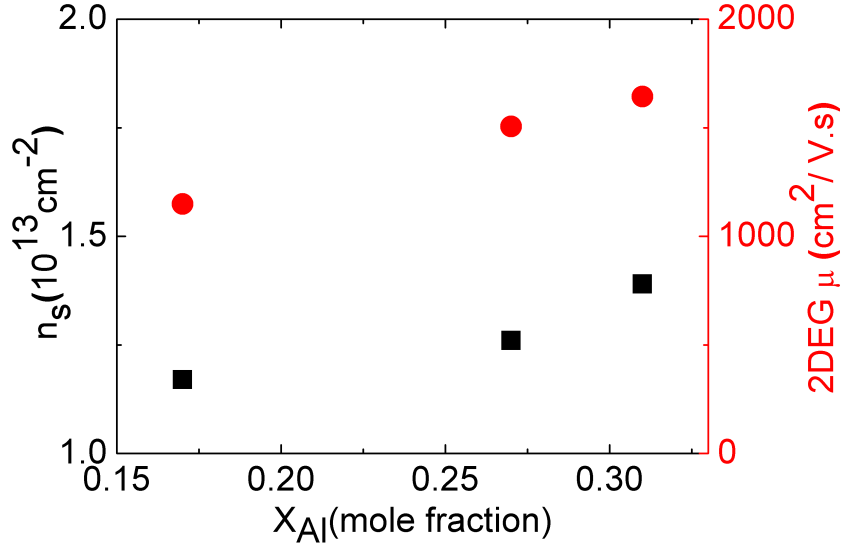


Figure 4.9: Sheet carrier density and 2DEG mobility of HEMT samples as a function of Al content of AlGa_N.

carrier densities ($n_s > 1 \times 10^{13} \text{ cm}^2/\text{Vs}$) these mechanisms are screened so there is no deterioration in mobility [75, 74, 76]. Al content change with the conduction band offset. It become smaller for lower Al content and larger for higher Al content. Since the carriers are located at the interface of the AlGa_N/Ga_N layers, carrier distribution spreads into Ga_N layer for AlGa_N has a lower Al content. Electrons spill over towards the Ga_N and occupy the delocalized states in Ga_N, which reduces the electron mobility and lower the carrier density in case of lower Al content [74, 77].

As mentioned before, the product of $n_s \times \mu$ is a key parameter which correlates the sheet resistance for high power and high speed performance of HEMTs. Sheet resistances and $n_s \times \mu$ product values are calculated for the samples H1, H2, H3 as 2.28×10^{16} , 1.89×10^{16} , $1.34 \times 10^{16} / \text{V.s}$ and 273, 329, 464 Ω/\square , respectively. The highest values of $n_s \times \mu$ product and the lowest sheet resistances belong to Sample H1 and H2. Therefore, these structures are used for the fabrication of HEMT devices.

4.3 Characterizations of HEMT devices

Sample H1 and H2 HEMT structures are fabricated according to the process steps explained in the Chapter 3. The first electrical characterization is performed to obtain contact resistance (R_c) of ohmic contacts using the graphs given in Figure 4.10 and 4.11. Ohmic contact resistance is an important parameter to determine the performance of HEMT devices especially for high power applications. This is because the power losses increase with high ohmic contact resistances. AlGa_xN barrier thickness, 2DEG mobility and the contact resistances are measured by four-point TLM method from TLM patterns on the devices and found to be 0.47 Ω mm and 0.36 Ω mm for sample H1 and H2, respectively. These values are found to be in good agreement with the literature [78, 79, 68]. As Al content of the AlGa_xN barrier is increased, the contact resistance is increased due to the increase in the bandgap of AlGa_xN.

The second characterization is done to get the actual length of gate metals. A RAITH E-line system is used for this purpose. A SEM images of the gate is provided in Figure 4.12. SEM image revealed that the gate length is around 300 nm.

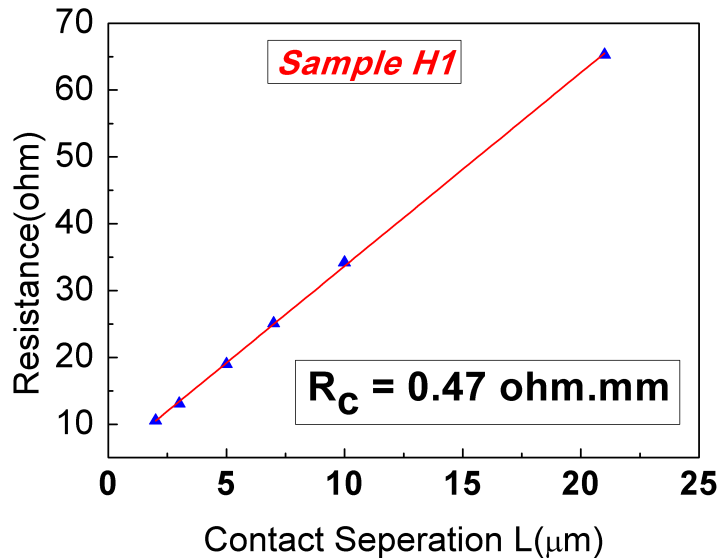


Figure 4.10: TLM data measured by four point probe method for sample H1.

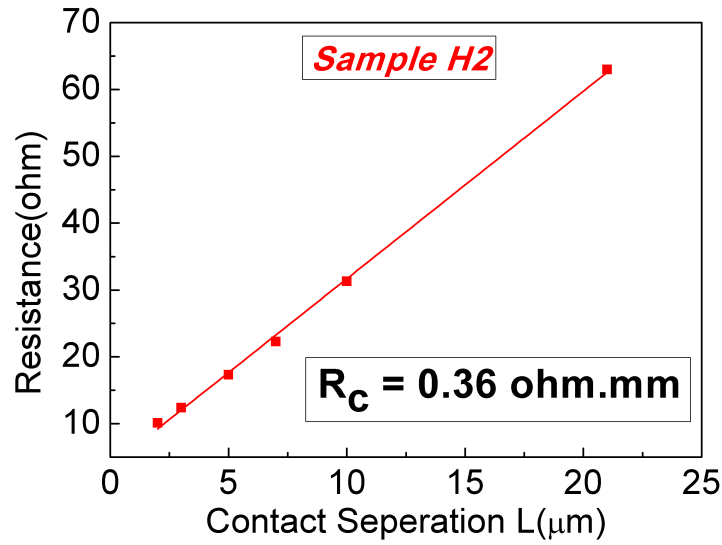


Figure 4.11: TLM data measured by four point probe method for sample H2.

Finally, following the passivation step, the refractive index and the thickness of the Si_3N_4 thin film is measured by SENTECH 850 SE850 ellipsometry system. The thickness and refractive index of the films are determined to be 296 nm and 1.97, respectively. These values are also found to be consistent with the literature [80].

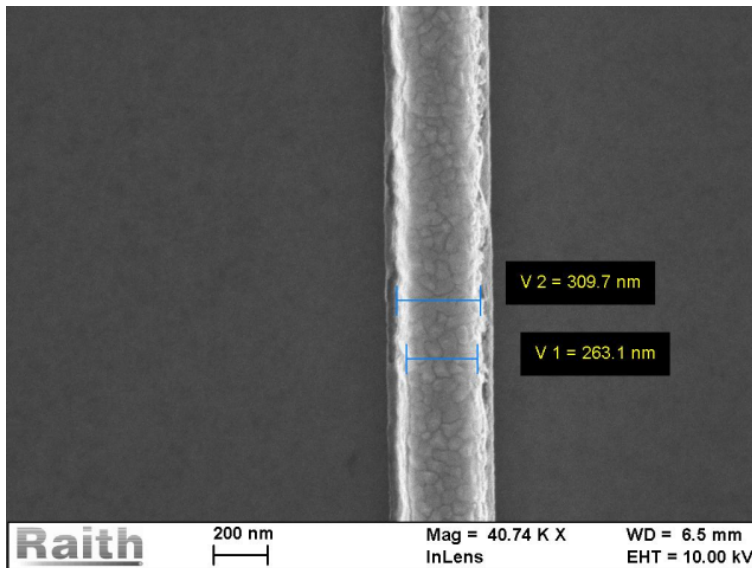


Figure 4.12: SEM image of the gate metal.

4.4 DC Characterization of fabricated HEMT devices

In this section DC output and transfer characteristics of fabricated samples H1 and H2 will be discussed. $4 \times 75 \mu\text{m}$ HEMT devices with a gate length (L_G) of 300 nm and source to drain distance (L_{sd}) of $3 \mu\text{m}$ are fabricated and analysed. Agilent B1505A power device analyser and Cascade M150 probe station are used to perform DC measurements. Obtained DC characteristics of samples H1 and H2 are provided in Figure 4.13, 4.14, 4.15.

Important parameters such as knee voltage (V_{knee}), pinch-off voltage (V_p), breakdown voltage (V_{br}), maximum drain current density ($I_{DS,max}$) and peak transconductance ($g_{m,max}$) are determined from output, transfer and breakdown characteristics graphs. DC output characteristics are measured up to a 10 V drain to source voltage, while sweeping the gate voltage from 1 to -6 V. At a gate voltage of -6 V all transistors were pinched-off. Maximum drain current per area is found as 1210 mA/mm and 710 mA/mm for H1 and H2, respectively, while the knee voltages were 6.2 V and 5.4 V. For measuring the DC transconductance, drain voltage is fixed at the knee voltage and gate voltage is swept while drain current is recorded. Peak transconductance values are obtained as 288 mS/mm and 217

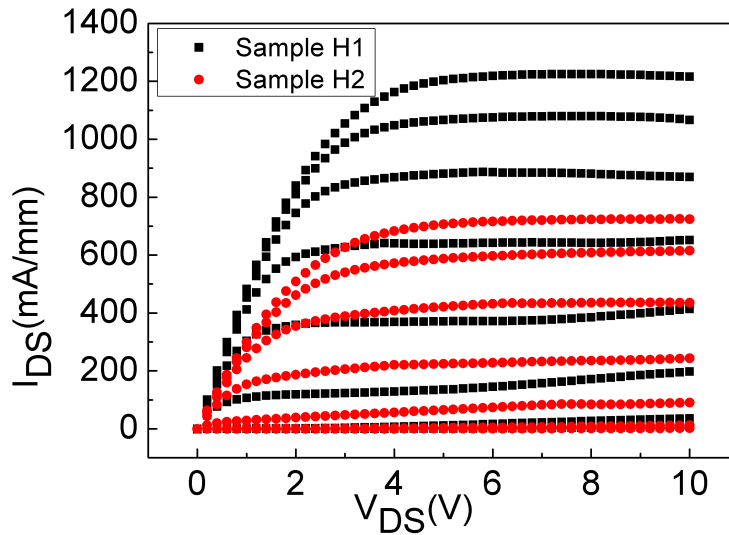


Figure 4.13: DC output characteristic of sample H1 and H2.

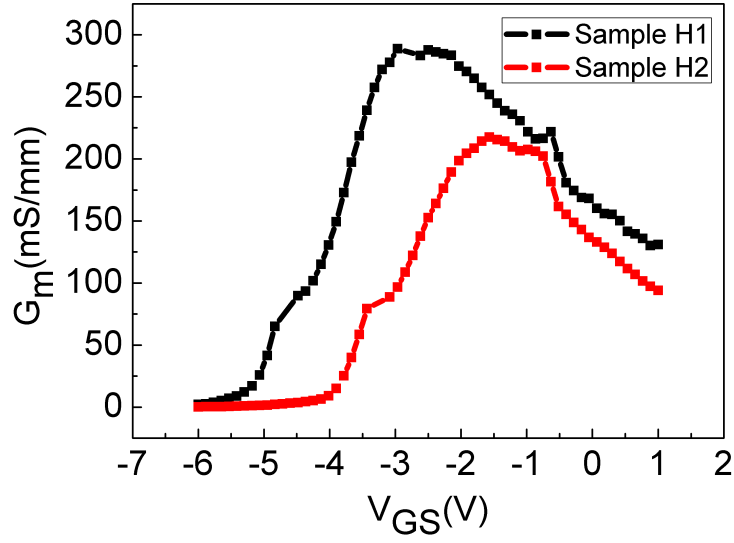


Figure 4.14: DC transfer characteristics of sample H1 and H2.

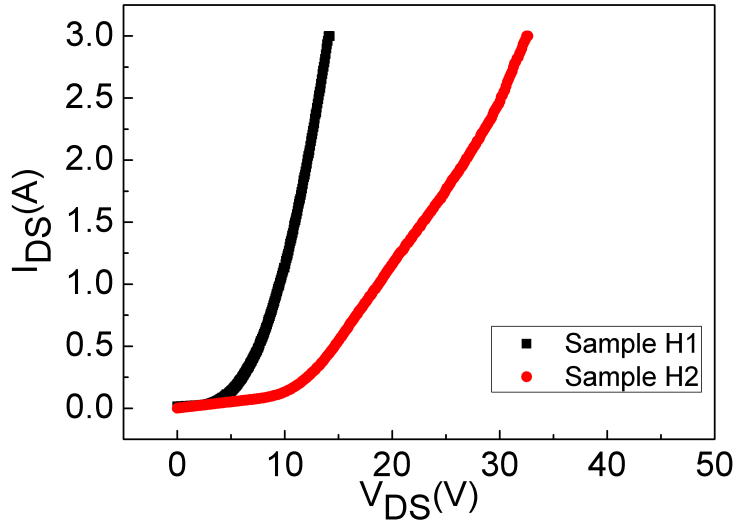


Figure 4.15: Breakdown voltage characteristics of sample H1 and H2.

mS/mm for H1 and H2, respectively. Another parameter, breakdown voltage is obtained from measuring the drain current while increasing the drain voltage until 10 mA/mm drain current density is achieved. Meanwhile, gate voltage is kept constant at less than a pinch-off voltage value. Breakdown voltages are obtained as 14 V and 32 V for H1 and H2, respectively.

The maximum drain current density and peak transconductance values are both increased with Al content. This can be explained by the increase both in mobility and sheet carrier density. Furthermore, breakdown voltage decreases with the Al content, this difference can be explained by the higher resistivity of GaN buffer layer for Sample H2 (lower Al content). The resistivity value can be foresaw from the HRXRD measurement results, which indicated a larger FWHM peak of AlN (102). Larger FWHM peak of AlN(102) is a sign of higher edge-type dislocation density which directly related to higher resistivity. As GaN buffer resistivity increased, gate leakage decreased and hence, breakdown voltage is increased. It is also possible that passivation may lead to a decrease in both maximum drain current density and transconductance for sample H2. Decrease in maximum drain current density and transconductance is reported [81].

The best drain current density, peak transconductance and $n_s \times \mu$ product value is obtained from sample H1 (Al mole fraction of 31%) as 1210 mA/mm, 288 mS/mm and 2.28×10^{16} , respectively. These results are found to be consistent with the literature. Some promising device performances obtained from literature together with sample H1 and H2 are provided in Table 4.4. Generally, the device characteristics (maximum drain current density, transconductance and breakdown voltage) varied due to the following factors: epitaxial layers quality (surface roughness, 2DEG mobility and 2DEG carrier concentration, sheet resistance), deposition type, ohmic contact resistance, substrate, surface passivation or fabrication geometries (gate length, drain to source distance) and device design (field-plate or T-gate).

Table 4.4: Literature review of AlGa_N/Ga_N HEMT device performances.

L_G, W_G μm	Method/Substrate	Al (%)	n_s (cm^{-2})	μ ($\text{cm}^2/\text{V}\cdot\text{s}$)	R_{sh} (Ω/\square)	R_c $\Omega\cdot\text{mm}$	$I_{DS,max}$ mA/mm	G_{max} mS/mm	Ref.
0.7, 2x75	MOCVD/ Al_2O_3	34	1.45×10^{13}	1650	250	0.30	2100	-	[82]
0.06, 2x25	MBE/SiC	-	8.00×10^{12}	2200	356	0.15	1200	410	[83]
0.06, 2x50	MOCVD/4H-SiC	40	1.70×10^{13}	2000	220	0.30	1600	424	[84]
0.35, 1000	MOCVD/6H-SiC	34	1.04×10^{13}	2215	251	0.40	1300	314	[85]
0.045, 2x50	MOCVD/SiC	26	9.10×10^{13}	1710	-	-	1263	274	[86]
0.3, 2x125	MOCVD/SiC	30	1.40×10^{13}	1200	450	0.30	1200	360	[87]
0.12, 100	MOCVD/4H-SiC	25	1.10×10^{13}	1300	-	0.35	1230	314	[88]
0.05, 200	MBE/SiC	-	1.10×10^{13}	1110	-	-	1200	110	[86]
0.25, 100	MOCVD/6H-SiC	30	-	-	380	0.15	1280	310	[89]
0.25, 100	MOCVD/4H-SiC	25	1.10×10^{13}	1300	275	0.35	1300	275	[90]
0.1, 150	MOCVD/SiC	32	1.50×10^{13}	1240	-	-	1400	380	[91]
0.14, 2x150	MOCVD/4H-SiC	34	1.14×10^{13}	1883	295	0.24	1481	338	[92]
0.3, 4x75	MOCVD/6H-SiC	31	1.39×10^{13}	1643	273	0.47	1210	288	Sample H1
0.3, 4x75	MOCVD/6H-SiC	27	1.26×10^{13}	1506	329	0.36	710	217	Sample H2

CHAPTER 5

CONCLUSIONS AND FUTURE WORK

The aim of this thesis is to grow, characterize and fabricate AlGa_xN/GaN HEMT structures on SiC substrates. The required properties of a good HEMT device are described as a highly resistive GaN buffer layer, a conductive channel layer which is correlated to the $n_s \times \mu$ product, good crystal quality and low surface roughness.

At first, nucleation layer parameters are optimized. Low temperature AlN nucleation layer thickness and annealing time are simultaneously varied, while keeping the other growth parameters such as temperature, pressure, V/III ratio, carrier gases constant. Both in-situ and ex-situ characterizations are conducted. The results indicated that highly resistive GaN layers with good crystal quality and smooth surfaces can be achieved.

Subsequently, optimized highly resistive GaN sample is used as a buffer and full HEMT structures are grown with varying Al concentration between 17 to 31 % of Al_xGa_(1-x)N barrier layer. Electrical characterizations revealed a successful 2DEG in all samples with good carrier concentration and mobility. It is found that, both the sheet carrier concentration and mobility increases with Al mole fraction. Structural characterizations indicated high crystal and interface qualities.

In the last part, two HEMT structures with high $n_s \times \mu$ product is fabricated and characterized. Consecutive sample preparation, mesa isolation, ohmic contact formation, Schottky contact formation, 1st level metallization, passivation,

contact pad opening, air-bridge formation and interconnect metallization steps are followed for the fabrication of HEMT devices. Devices with 4 x 75 fingers, 300 nm gate length and 0.3 μm source to drain distance are fabricated. The DC characterizations are performed. Maximum drain current density, peak transconductance and breakdown voltage of 1210 mA/mm, 288 mS/mm and 14 V are obtained from sample with 31 % Al content, respectively.

Obtained results have shown that these devices can be good candidate for high power, high frequency and high temperature electronic applications. However, further improvements and fine tuning is crucial for a specific application.

For future work, investigation of RF properties for better understanding the reason for current collapse and surface passivation effects would be important. In parallel, devices with different geometries can be fabricated and characterized, especially the effect of gate length, source to drain distance, number of fingers on the DC and RF characteristics would yield valuable information on HEMT devices.

Another approach can be further increasing the Al content of the AlGaN layer, where consecutively the modified material and device properties needs to be measured.

REFERENCES

- [1] D. Zhu, D. J. Wallis, and C. J. Humphreys, "Prospects of III-nitride optoelectronics grown on Si," *Reports Prog. Phys.*, vol. 76, p. 106501, Oct. 2013.
- [2] M. Golio, *RF and Microwave Semiconductor Handbook*. Florida: CRC Press, 2002.
- [3] S. Taking, *AlN/GaN MOS-HEMTs Technology*. PhD thesis, University of Glasgow, 2012.
- [4] Y. C. Liang, G. S. Samudra, H. Huang, C. F. Huang, and T. F. Chang, "Al-GaN/GaN power HEMT devices for future energy conversion applications," *2013 Int. Symp. Next-Generation Electron.*, pp. 7–10, Feb. 2013.
- [5] M. A. di Forte Poisson, M. Magis, M. Tordjman, R. Aubry, N. Sarazin, M. Peschang, E. Morvan, S. Delage, J. di Persio, R. Quéré, B. Grimbert, V. Hoel, E. Delos, D. Ducatteau, and C. Gaquiere, "LP-MOCVD growth of GaAlN/GaN heterostructures on silicon carbide: application to HEMT devices," *J. Cryst. Growth*, vol. 272, pp. 305–311, Dec. 2004.
- [6] R. S. Pengelly, S. M. Wood, J. W. Milligan, S. T. Sheppard, and W. L. Pribble, "A review of GaN on SiC high electron-mobility power transistors and MMICs," *IEEE Trans. Microw. Theory Tech.*, vol. 60, pp. 1764–1783, June 2012.
- [7] H. Morkoc, *Nitride Semiconductors Devices*, vol. 32. Springer Berlin Heidelberg, 1999.
- [8] O. Ambacher, J. Smart, J. R. Shealy, N. G. Weimann, K. Chu, M. Murphy, W. J. Schaff, L. F. Eastman, R. Dimitrov, L. Wittmer, M. Stutzmann, W. Rieger, and J. Hilsenbeck, "Two-dimensional electron gases induced by spontaneous and piezoelectric polarization charges in N- and Ga-face AlGaIn/GaN heterostructures," *J. Appl. Phys.*, vol. 85, no. 6, p. 3222, 1999.
- [9] S. Sze and K. N. Kwok, *Physics of Semiconductor Devices*. John Wiley and Sons, 3rd ed., 2007.
- [10] J. Bernat, *Fabrication and characterisation of AlGaIn/GaN high electron mobility transistors for power applications*. PhD thesis, RWTH Aachen, 2005.
- [11] W. Brinkman, D. Haggan, and W. Troutman, "A history of the invention of the transistor and where it will lead us," *IEEE J. Solid-State Circuits*, vol. 32, no. 12, pp. 1858–1865, 1997.

- [12] R. Ross, S. Svensson, and P. Lugli, *Pseudomorphic HEMT Technology and Applications*. Dordrecht-Boston-London: Kluwer Academic Publisher, 1996.
- [13] T. Mimura, "The early history of the high electron mobility," *IEEE Trans. Magn.*, vol. 50, no. 3, pp. 780–782, 2002.
- [14] T. Mimura, S. Hiyamizu, T. Fujii, and K. Nanbu, "A new field-effect transistor with selectively doped GaAs/n-Al_xGa_(1-x)As heterojunctions," *Jpn. J. Appl. Phys.*, vol. 19, pp. L225–L227, 1980.
- [15] M. Fukuta, "History of HEMT Transistors," *Fujutsi Quantum Ltd. Ed.*, p. 1998, 1998.
- [16] G. P. Pal and A. K. Shrivastav, "High electron mobility transistor(HEMT)," *Int. J. Sci. Res. Eng. Technol.*, vol. 1, no. March, pp. 43–46, 2012.
- [17] H. Amano, N. Sawaki, I. Akasaki, and Y. Toyoda, "Metalorganic vapor phase epitaxial growth of a high quality GaN film using an AlN buffer layer," *Appl. Phys. Lett.*, vol. 48, p. 353, Feb. 1986.
- [18] M. A. Khan, A. Bhattarai, J. N. Kuznia, and D. T. Olson, "High electron mobility transistor based on a GaN/Al_xGa_(1-x)N heterojunction," *Appl. Phys. Lett.*, vol. 63, no. 9, p. 1214, 1993.
- [19] M. A. Khan, J. N. Kuznia, J. M. Van Hove, D. T. Olson, S. Krishnankutty, and R. M. Kolbas, "Growth of high optical and electrical quality GaN layers using low-pressure metalorganic chemical vapor deposition," *Appl. Phys. Lett.*, vol. 58, no. 5, p. 526, 1991.
- [20] S. Nakamura, Y. Harada, and M. Seno, "Novel metalorganic chemical vapor deposition system for GaN growth," *Appl. Phys. Lett.*, vol. 58, no. 18, p. 2021, 1991.
- [21] F. Conti and M. Conti, "Surface breakdown in silicon planar diodes equipped with field plate," *Solid. State. Electron.*, vol. 15, pp. 93–105, Jan. 1972.
- [22] R. Wang, *Enhancement/depletion-mode HEMT technology for III-nitride mixed-signal RF applications*. PhD thesis, The Hong Kong University of Science and Technology, 2008.
- [23] M. A. Acar, "Fabrication, modeling and characterization of GaN HEMTs, and design of high power MMIC amplifiers," Master's thesis, Bilkent University, 2009.
- [24] S. R. Lee, A. F. Wright, M. H. Crawford, G. A. Petersen, J. Han, and R. M. Biefeld, "The band-gap bowing of AlGa_xN/GaN alloys," *Appl. Phys. Lett.*, vol. 74, no. 22, p. 3344, 1999.
- [25] Y. Koide, H. Itoh, M. R. H. Khan, K. Hiramatu, N. Sawaki, and I. Akasaki, "Energy band-gap bowing parameter in an Al_xGa_(1-x)N alloy," *J. Appl. Phys.*, vol. 61, no. 9, p. 4540, 1987.

- [26] L. Guo, X. X. Wang, C. Wang, H. Xiao, J. Ran, W. Luo, B. Wang, C. Fang, and G. Hu, "The influence of 1nm AlN interlayer on properties of the $\text{Al}_{0.3}\text{Ga}_{0.7}\text{N}/\text{AlN}/\text{GaN}$ HEMT structure," *Microelectronics J.*, vol. 39, pp. 777–781, May 2008.
- [27] Z. Y. Ma, Z. L. Wang, G. X. Hu, J. X. Ram, H. L. Xiao, W. J. Luo, J. Tang, J. P. Li, and J. M. Li, "Growth and characterization of AlGaN/AlN/GaN HEMT structures with a compositionally step-graded AlGaN barrier layer," *Chinese Phys. Lett.*, vol. 24, no. 6, pp. 1705–1708, 2007.
- [28] L. Shen, S. Heikman, B. Moran, R. Coffie, N.-Q. Zhang, D. Buttari, I. Smorchkova, S. Keller, S. DenBaars, and U. Mishra, "AlGaN/AlN/GaN high-power microwave HEMT," *IEEE Electron Device Lett.*, vol. 22, pp. 457–459, Oct. 2001.
- [29] X. Wu, P. Fini, S. Keller, E. Tarsa, B. Heying, U. Mishra, S. DenBaars, and J. Speck, "Morphological and structural transitions in GaN films grown on sapphire by metal-organic chemical vapor deposition," *Jpn. J. Appl. Phys.*, vol. 35, pp. 1648–1651, 1996.
- [30] L. Eastman, V. Tilak, J. Smart, B. Green, E. Chumbes, R. Dimitrov, O. Ambacher, N. Weimann, T. Prunty, M. Murphy, W. Schaff, and J. Shealy, "Undoped AlGaN/GaN HEMTs for microwave power amplification," *IEEE Trans. Electron Devices*, vol. 48, pp. 479–485, Mar. 2001.
- [31] M. Rudzinski, *GaN grown on SiC by MOCVD*. PhD thesis, Radboud University Nijmegen, 2008.
- [32] I. Akasaki and H. Amano, "Crystal growth and conductivity control of group III nitride semiconductors and their application of short wavelength emitters," *Japan*, vol. 36, no. 5393-5408, 1997.
- [33] S. Heikman, S. Keller, S. P. DenBaars, and U. K. Mishra, "Growth of Fe doped semi-insulating GaN by metalorganic chemical vapor deposition," *Appl. Phys. Lett.*, vol. 81, no. 3, p. 439, 2002.
- [34] A. Grzegorzcyk, L. Macht, P. Hageman, J. Weyher, and P. Larsen, "Influence of the nucleation layer morphology and epilayer structure on the resistivity of GaN films grown on c-plane sapphire by MOCVD," *J. Cryst. Growth*, vol. 273, pp. 424–430, Jan. 2005.
- [35] A. Jones and P. O'Brien, *CVD of compound semiconductors: precursor synthesis, development and applications*. Wiley-VCH, 1 ed., 1997.
- [36] M. Razeghi, *The MOCVD Challenge: Volume 2: A Survey of GaInAsP-GaAs for Photonic and Electronic Device Applications*. 1995.
- [37] N. E. Kaluza, *MOVPE growth and characterization of AlGaN/GaN heterostructures for HEMT application*. PhD thesis, 2003.
- [38] A. Lundskog, *Characterization of advanced AlGaN HEMT structures*. PhD thesis, Linköping university, 2007.

- [39] P. Javorka, *Fabrication and characterization of AlGaN/GaN high electron mobility transistors*. PhD thesis, RWTH Aachen, 2004.
- [40] K. Haberland, *Optical in-situ studies during MOVPE with respect to III-V device production*. PhD thesis, Technische Universität Berlin, 2002.
- [41] “Reflectance measurements for real-time optical control of epitaxial growth,” *Laytec Inf. Notes*, 2008.
- [42] C. Kaspari, *Fast optical in situ spectroscopy in III-V MOVPE*. PhD thesis, Technischen Universität Berlin, 2007.
- [43] P. F. Fewster, *X-Ray Scattering From Semiconductors*. Imperial College Press, 2003.
- [44] “<http://prism.mit.edu/xray/tutorials.htm>, last visited on 8th of January 2014.”
- [45] H. Ibach and H. Lüth, *Solid-State Physics*. Berlin, Heidelberg: Springer Berlin Heidelberg, 2009.
- [46] “http://www.nist.gov/pml/div683/hall_fig4.cfm, last visited on 8th of January 2014.”
- [47] L. Van Der Pauw, “A method of measuring specific resistivity and Hall coefficient on lamellae of arbitrary shape,” *Philips Tech. Rev.*, vol. 20, pp. 220–224, 1958.
- [48] A. Hamilton and F. Quail, “Detailed State of the Art Review for the Different Online/Inline Oil Analysis Techniques in Context of Wind Turbine Gearboxes,” *J. Tribol.*, vol. 133, no. 4, p. 044001, 2011.
- [49] T. Ito and S. Okazaki, “Pushing the limits of lithography,” *Nature*, vol. 406, pp. 1027–31, Aug. 2000.
- [50] M. Kirchner and M. Kahl, “Raith — Electron beam lithography for research,” in *Proc. III Natl. Conf. Nanotechnol. NANO 2009*, vol. 116, pp. 198–200, 2009.
- [51] M. A. McCord and M. J. Rooks, *Handbook of Microlithography, Micromachining and Microfabrication*, vol. 1. SPIE Press, 1997.
- [52] Y. F. Wu, D. Kapolnek, D. P. Ibbetson, P. Parikh, B. Keller, and U. K. Mishra, “Very-high power density AlGaIn/GaN HEMTs,” *Electron Devices, IEEE Trans.*, vol. 48, no. 3, pp. 586–590, 2001.
- [53] S. Hubbard, D. Pavlidis, V. Valiaev, and A. Eisenbach, “Metal-organic vapor phase epitaxy growth and characterization of AlN/GaN heterostructures,” *J. Electron. Mater.*, vol. 31, pp. 395–401, 2002.
- [54] W. Wang, Y. Li, C. Lin, Y. Chan, G. Chen, and J. Chyi, “Low damage, Cl₂ based gate recess etching for 0.3 μm gate-length AlGaIn/ GaN HEMT fabrication,” *IEEE Electron Device Lett.*, vol. 25, no. 2, pp. 52–54, 2004.

- [55] S. A. Smith, C. A. Wolden, M. D. Bremser, A. D. Hanser, R. F. Davis, and W. Lampert V., "High rate and selective etching of GaN, AlGa_N, and AlN using an inductively coupled plasma," *Appl. Phys. Lett.*, vol. 71, no. 25, pp. 3631–3633, 1997.
- [56] T. Uesugi, T. Okada, A. Wada, K. Kato, A. Yasuda, S. Maeda, and S. Samukawa, "The effects of polymer side-chain structure on roughness formation of ArF photoresist in plasma etching processes," *J. Phys. D. Appl. Phys.*, vol. 45, p. 075203, Feb. 2012.
- [57] D. E. Wolfe and J. Singh, "Titanium carbide coatings deposited by reactive ion beam-assisted, electron beam–physical vapor deposition," *Surf. Coatings Technol.*, vol. 124, no. 2, pp. 142–153, 2000.
- [58] S. Franssila, *Introduction to Microfabrication*. John Wiley and Sons, 2004.
- [59] G. S. Mathad, D. W. Hess, and M. Meyyappan, "Plasma processing for silicon-based integrated circuits," *Electrochem. Soc. Interface*, 1999.
- [60] D. Sawdai, D. Pavlidis, and D. Cui, "Enhanced transmission line model structures for accurate resistance evaluation of small-size contacts and for more reliable fabrication," *IEEE Trans. Electron Devices*, vol. 46, no. 7, p. 1999, 1999.
- [61] D. Selvanathan, F. M. Mohammed, A. Tesfayesus, and I. Adesida, "Comparative study of Ti/Al/Mo/Au, Mo/Al/Mo/Au, and V/Al/Mo/Au ohmic contacts to AlGa_N/Ga_N heterostructures," *J. Vac. Sci. Technol. B Microelectron. Nanom. Struct.*, vol. 22, p. 2409, Oct. 2004.
- [62] E. D. Palik, *A Handbook of Optical Constants of Solids*. Orlando: Academic Press, 1985.
- [63] Z. Zhou, L. Guo, Z. Xing, G. Ding, J. Zhang, M. Peng, H. Jia, H. Chen, and J. Zhou, "Growth of semi-insulating Ga_N by using two-step AlN buffer layer," *Chinese Phys. Lett.*, vol. 24, no. 6, p. 1641, 2007.
- [64] Z. Zhou, Z. Xing, L. Guo, H. Chen, and J. Zhou, "Growth of semi-insulating Ga_N using N₂ as nucleation layer carrier gas combining with an optimized annealing time," *Chinese Phys. B*, vol. 24, no. 6, p. 1645, 2007.
- [65] R. Gaska, J. W. Yang, A. Osinsky, Q. Chen, M. A. Khan, A. O. Orlov, G. L. Snider, and M. S. Shur, "Electron transport in AlGa_N-Ga_N heterostructures grown on 6H-SiC substrates," *Appl. Phys. Lett.*, vol. 72, no. 6, p. 707, 1998.
- [66] F. M. Mohammed, L. Wang, and I. Adesida, "Noninterfacial-nitride formation ohmic contact mechanism in Si-containing Ti/Al/Mo/Au metallizations on AlGa_N/Ga_N heterostructures," *Appl. Phys. Lett.*, vol. 87, no. 26, p. 262111, 2005.
- [67] L. Wang, F. M. Mohammed, and I. Adesida, "Differences in the reaction kinetics and contact formation mechanisms of annealed Ti/Al/Mo/Au ohmic contacts on n-Ga_N and AlGa_N/Ga_N epilayers," *J. Appl. Phys.*, vol. 101, no. 1, p. 013702, 2007.

- [68] K. H. Kim, C. M. Jeon, S. H. Oh, J. L. Lee, C. G. Park, J. H. Lee, K. S. Lee, and Y. M. Koo, "Investigation of Ta/Ti/Al/Ni/Au ohmic contact to AlGa_N/Ga_N heterostructure field-effect transistor," *J. Vac. Sci. Technol. B Microelectron. Nanom. Struct.*, vol. 23, no. 1, p. 322, 2005.
- [69] R. F. Davis, S. M. Bishop, S. Mita, R. Collazo, Z. J. Reitmeier, and Z. Sitar, "Epitaxial growth of gallium nitride," *AIP Conf. Proc.*, vol. 916, pp. 520–540, 2007.
- [70] B. Heying, X. H. Wu, S. Keller, Y. Li, D. Kapolnek, B. P. Keller, S. P. DenBaars, and J. S. Speck, "Role of threading dislocation structure on the x-ray diffraction peak widths in epitaxial Ga_N films," *Appl. Phys. Lett.*, vol. 68, no. 5, p. 643, 1996.
- [71] M. A. Moram and M. E. Vickers, "X-ray diffraction of III-nitrides," *Reports Prog. Phys.*, vol. 72, p. 036502, Mar. 2009.
- [72] D. Green, S. Gibb, B. Hosse, R. Vetury, D. Grider, and J. Smart, "Control of epitaxial defects for optimal AlGa_N/Ga_N HEMT performance and reliability," *J. Cryst. Growth*, vol. 272, pp. 285–292, Dec. 2004.
- [73] H. Amano, M. Iwaya, N. Hayashi, T. Kashima, S. Nitta, C. Wetzel, and I. Akasaki, "Control of dislocations and stress in AlGa_N on sapphire using a low temperature Interlayer," *Phys. Status Solidi*, vol. 216, pp. 683–689, Nov. 1999.
- [74] S. Arulkumaran, T. Egawa, H. Ishikawa, and T. Jimbo, "Characterization of different-Al-content AlGa_N/Ga_N heterostructures and high-electron-mobility transistors on sapphire," *J. Vac. Sci. Technol. B Microelectron. Nanom. Struct.*, vol. 21, pp. 888–894, 2003.
- [75] I. P. Smorchkova, C. R. Elsass, J. P. Ibbetson, R. Vetury, B. Heying, P. Fini, E. Haus, S. P. DenBaars, J. S. Speck, and U. K. Mishra, "Polarization-induced charge and electron mobility in AlGa_N/Ga_N heterostructures grown by plasma-assisted molecular-beam epitaxy," *J. Appl. Phys.*, vol. 86, no. 8, p. 4520, 1999.
- [76] K. Kohler, S. Muller, P. Waltereit, L. Kirste, H. P. Menner, W. Bronner, and R. Quay, "Growth and electrical properties of Al_xGa_(1-x)N/Ga_N heterostructures with different Al-content," *Phys. Status Solidi*, vol. 206, pp. 2652–2657, Nov. 2009.
- [77] G. Zhao, H. Ishikawa, T. Egawa, T. Jimbo, and M. Umeno, "Electron mobility on AlGa_N/Ga_N heterostructure interface," *Phys. E Low-dimensional Syst. Nanostructures*, vol. 7, pp. 963–966, May 2000.
- [78] Y. Sun, X. Chen, and L. F. Eastman, "Comprehensive study of ohmic electrical characteristics and optimization of Ti/Al/Mo/Au multilayer ohmics on undoped AlGa_N/Ga_N heterostructure," *J. Appl. Phys.*, vol. 98, no. 5, p. 053701, 2005.
- [79] L. Wang, D. H. Kim, and I. Adesida, "Direct contact mechanism of ohmic metallization to AlGa_N/Ga_N heterostructures via ohmic area recess etching," *Appl. Phys. Lett.*, vol. 95, no. 17, p. 172107, 2009.

- [80] T. Baak, "Silicon oxynitride; a material for GRIN optics," *Appl. Opt.*, vol. 21, pp. 1069–1072, 1982.
- [81] W. Lu, V. Kumar, R. Schwindt, E. Piner, and I. Adesida, "A comparative study of surface passivation on AlGa_N/Ga_N HEMTs," *Solid State Electron.*, vol. 46, pp. 1441–1444, 2002.
- [82] A. Chini, R. Coffe, G. Meneghesso, E. Zanoni, D. Buttari, S. Heikman, S. Keller, and U. K. Mishra, "2.1A/mm current density AlGa_N/Ga_N HEMT," vol. 39, no. 7, pp. 625–626, 2003.
- [83] J. W. Chung, W. E. Hoke, E. M. Chumbes, and T. Palacios, "AlGa_N/Ga_N HEMT with 300-GHz f_{max}," *IEEE Electron Device Lett.*, vol. 31, no. 3, pp. 195–197, 2010.
- [84] M. Higashiwaki, T. Mimura, and T. Matsui, "AlGa_N/Ga_N heterostructure field-effect transistors on 4H-SiC substrates with current-gain cutoff frequency of 190 GHz," *Appl. Phys. Express*, vol. 1, p. 021103, Feb. 2008.
- [85] X. Wang, G. Hu, Z. Ma, J. Ran, C. Wang, H. Xiao, J. Tang, J. Li, J. Wang, Y. Zeng, and Z. Wang, "AlGa_N/Al_N/Ga_N/SiC HEMT structure with high mobility Ga_N thin layer as channel grown by MOCVD," *J. Cryst. Growth*, vol. 298, pp. 835–839, Jan. 2007.
- [86] A. Endoh, I. Watanabe, Y. Yamashita, T. Mimura, and T. Matsui, "AlGa_N/Ga_N MIS-HEMTs with f_T of 194 GHz at 16 K," *Electron. Lett.*, vol. 44, no. 4, pp. 44–45, 2008.
- [87] V. Tilak, B. Green, V. Kaper, H. Kim, T. Prunty, J. Smart, J. Shealy, and L. Eastman, "Influence of barrier thickness on the high-power performance of AlGa_N/Ga_N HEMTs," *IEEE Electron Device Lett.*, vol. 22, no. 11, pp. 504–506, 2001.
- [88] V. Kumar, W. Lu, R. Schwindt, A. Kuliev, G. Simin, J. Yang, M. Asif Khan, and I. Adesida, "AlGa_N/Ga_N HEMTs on SiC with f_T of over 120 GHz," *IEEE Electron Device Lett.*, vol. 23, pp. 455–457, Aug. 2002.
- [89] V. Kumar, J. Lee, A. Kuliev, O. Aktas, R. Schwindt, R. Birkhahn, D. Gotthold, S. Guo, B. Albert, and I. Adesida, "AlGa_N/Ga_N HEMTs on 6H-SiC with power density of 6.7 W/mm at 18 GHz," *Electron. Lett.*, vol. 39, no. 22, pp. 21–22, 2003.
- [90] R. Schwindt, V. Kumar, A. Kuliev, G. Simin, J. W. Yang, M. A. Khan, M. E. Muir, and I. Adesida, "AlGa_N/Ga_N HEMTs on SiC substrates," *IEEE Microw. Wirel. Components Lett.*, vol. 13, no. 3, pp. 93–95, 2003.
- [91] T. Palacios, Y. Dora, a. Chakraborty, C. Sanabria, S. Keller, S. P. DenBaars, and U. K. Mishra, "Optimization of AlGa_N/Ga_N HEMTs for high frequency operation," *Phys. Status Solidi*, vol. 203, pp. 1845–1850, May 2006.
- [92] G. H. Jessen, R. C. Fitch, J. K. Gillespie, G. D. Via, N. A. Moser, M. J. Yannuzzi, A. Crespo, J. S. Sewell, R. W. Dettmer, T. J. Jenkins, R. F.

Davis, J. Yang, M. A. Khan, and S. C. Binari, "AlGa_N/Ga_N power HEMTs on SiC," *IEEE Electron Device Lett.*, vol. 24, no. 11, pp. 677–679, 2003.